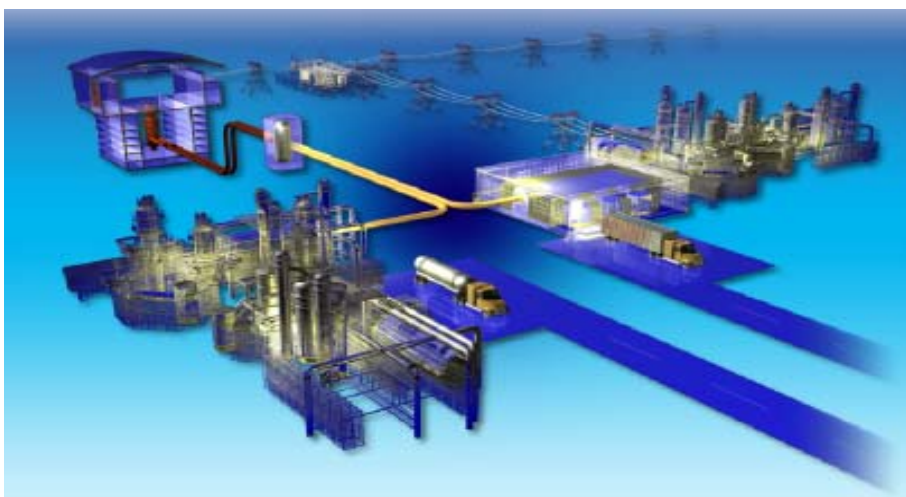# Deterministic Modeling of the High Temperature Test Reactor

Javier Ortensi
Joshua J. Cogliati
Michael A. Pope
John D. Bess
Rodolfo M. Ferrer
Avery A. Bingham
Abderrafi M. Ougouag

June 2010

The INL is a U.S. Department of Energy National Laboratory
operated by Battelle Energy Alliance

Deterministic Modeling of the High Temperature Test Reactor

Javier Ortensi, Joshua J. Cogliati, Michael A. Pope, John D. Bess, Rodolfo M. Ferrer, Avery A. Bingham, Abderrafi M. Ougouag

June 2010

Idaho National Laboratory
Next Generation Nuclear Plant Project
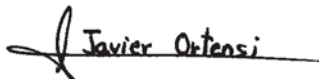**Idaho Falls, Idaho 83415**

Next Generation Nuclear Plant Project

Deterministic Modeling of the High Temperature Test Reactor

INL/EXT-10-18969

June 2010

Approved by:
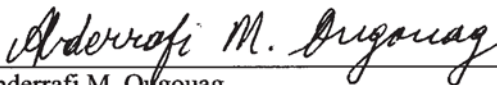
Javier Ortensi   06/28/2010

Javier Ortensi   Date
NGNP Physics

Abderrafi M. Ougouag   06/28/2010

Abderrafi M. Ougouag   Date
NGNP Physics Technical Lead

Hans Gougar   06/28/2010
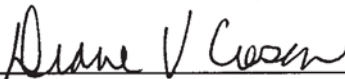
Hans Gougar   Date
NGNP Technical Deputy Director

Diane V Croson   6/28/10

Diane Croson   Date
NGNP Deputy Director

Abstract

Idaho National Laboratory (INL) is tasked with the development of reactor physics analysis capability for the Next Generation Nuclear Power (NGNP) project. In order to examine INL's current prismatic reactor deterministic analysis tools, the project is conducting a benchmark exercise based on modeling the High Temperature Test Reactor (HTTR). This exercise entails the development of a model for the initial criticality, a 19-fuel column thin annular core, and the fully loaded core critical condition with 30 fuel columns. Special emphasis is devoted to the annular core modeling, which shares more characteristics with the NGNP base design. The DRAGON code is used in this study because it offers significant ease and versatility in modeling prismatic designs. Despite some geometric limitations, the code performs quite well compared to other lattice physics codes. DRAGON can generate transport solutions via collision probability (CP), method of characteristics (MOC), and discrete ordinates (Sn). A fine group cross-section library based on the SHEM 281 energy structure is used in the DRAGON calculations. HEXPEDITE is the hexagonal-z full-core solver used in this study and is based on the Green's Function solution of the transverse-integrated equations. In addition, two Monte Carlo (MC) based codes, MCNP5 and PSG2/SERPENT, as well as the deterministic transport code INSTANT, provide benchmarking capability for the DRAGON and HEXPEDITE. The results from this study show reasonable agreement in the calculation of the core multiplication factor with the MC methods, but a consistent bias of 2–3% with the experimental values is obtained. This systematic error has also been observed in other HTTR benchmark efforts and is well documented in the literature. The uncertainty in the graphite impurity appears to be the main source of the error, whereas inaccuracies in the ENDF/B-VII graphite and U_{235} cross-sections have a secondary effect. The isothermal temperature coefficients calculated with the fully loaded core configuration agree well with other benchmark participants but are 40% higher than the experimental values. This discrepancy with the measurement partially stems from the fact that during the experiments the control rods were adjusted to maintain criticality, whereas in the model, the rod positions were fixed. In addition, this work includes a brief study of a cross-section generation approach that seeks to decouple the domain in order to account for neighbor effects. This spectral interpenetration is a dominant effect in annular HTR physics. This analysis methodology should be further explored in order to reduce the error that is systematically propagated in the traditional generation of cross-sections.

CONTENTS

FIGURES

TABLES

ACRONYMS

BPs	burnable poisons
CFP	coated fuel particles
CP	collision probability
CR	control rod
DB	dummy block
DH	double heterogeneity
EFPD	effective full power days
FHH	fuel-handling hole
HGTR	high temperature gas-cooled reactor
HTR	high temperature reactor
HTTR	High Temperature Test Reactor
IAEA	International Atomic Energy Agency
INL	Idaho National Laboratory
IPyC	inner pyrolytic carbon
IRPhEP	International Reactor Physics Experiment Evaluation Project
ITC	isothermal temperature coefficient
JAEA	Japan Atomic Energy Agency
JAERI	Japan Atomic Energy Research Institute
MC	Monte Carlo
MCNP	Monte Carlo N-Particle Transport Code
MOC	method of characteristics
NGFM	Nodal Green's Function Method
NGNP	Next Generation Nuclear Plant
ODE	ordinary differential equation
OPyC	outer pyrolytic carbon
PyC	pyrolytic carbon
RR	replaceable reflector
RSS	reserve shutdown system
SiC	silicon carbide

Sn	discrete ordinates
TD	theoretical density
TRISO	tri-isotropic
V&V	verification and validation
VHTR	very high temperature reactor

Deterministic Modeling of the High Temperature Test Reactor

1. INTRODUCTION

The verification and validation (V&V) of nuclear codes is an integral part of a comprehensive methods and analysis tasks that take place before the licensing application of new nuclear reactor designs. The verification of a computer code is the process of determining that a model implementation accurately represents the developer's conceptual description of the model and the solution to the model [1]. Therefore, the verification task involves the confirmation that the equations included in the code are being solved with a certain degree of accuracy. This verification step is normally achieved with the use of equivalent or higher fidelity solutions either analytic, manufactured, or those obtained with other methods or codes that have already been verified. The validation of a computer code is the process of determining the degree to which a model is an accurate representation of the real world from the perspective of the intended uses of the model [1]. In this case, the validation task provides an assessment of the validity of these models to actually represent physical phenomena. At this last stage, comparisons with measured data provide the basis to determine the applicability of the computer code for a particular analysis.

Idaho National Laboratory (INL) is tasked with the improvement of current calculation methods and analysis approaches in support of the licensing of the NGNP. In this function the INL seeks to 1) determine the current state of the methods available to analyze prismatic HTRs and 2) find any significant gaps in the computation technology that could hinder NGNP deployment. V&V of current computational methods will provide the necessary information to ascertain their state of readiness and the location areas that need further development. The verification of nuclear codes is commonly performed by developers and it has become the main focus area in the research community. The validation of the codes requires experimental data, which is scarce and has become extremely difficult to generate in recent years. A previous assessment [2] suggested that the experiments conducted at the High Temperature Test Reactor (HTTR) constitute some of the best reactor physics measurements currently available in the open literature applicable to the prismatic NGNP.

Presently, this work must rely on publicly available data that might not contain all the necessary specifications or quality to produce accurate comparisons to the experiments. Better quality data might become available in the future as more emphasis is placed on the validation efforts for NGNP. The three central sources of information used in this work are the International Atomic Energy Agency (IAEA) working group report [3], the Japan Atomic Energy Research Institute (JAERI) benchmark definition memorandum [4], and the International Reactor Physics Experiment Evaluation Project (IRPhEP) reports [5,6]. This latter work represents the modeling task performed at the INL with probabilistic tools, i.e. Monte Carlo. The INL reports conclude that there are still significant questions regarding the quality of the HTTR data available in the public domain, especially in reaction rate distribution and rod worth measurements. Nevertheless, it is still useful to compare computational model results to experimental measurements, since the data can be used to validate some of the calculations that are necessary in the licensing application process. The first stage in the validation of neutronic codes, and the primary focus of this report, is the calculation of the core multiplication factor.

The deterministic modeling task is a complex endeavor that requires two distinct calculations. The first calculation is performed at the block or assembly level in what is traditionally called a lattice physics calculation (Figure 1). At this stage most of the geometric and material details that comprise the heterogeneous block are included in the calculation of the neutron flux. Homogenization theory is used to produce a set of cross-sections and diffusion coefficients. This calculation is typically performed for each block or assembly type in the core. The homogenized region cross-sections are subsequently input to a full core calculation shown in Figure 2. The main goal of this last computation is the determination of the core multiplication factor, flux, and power distributions throughout the core.
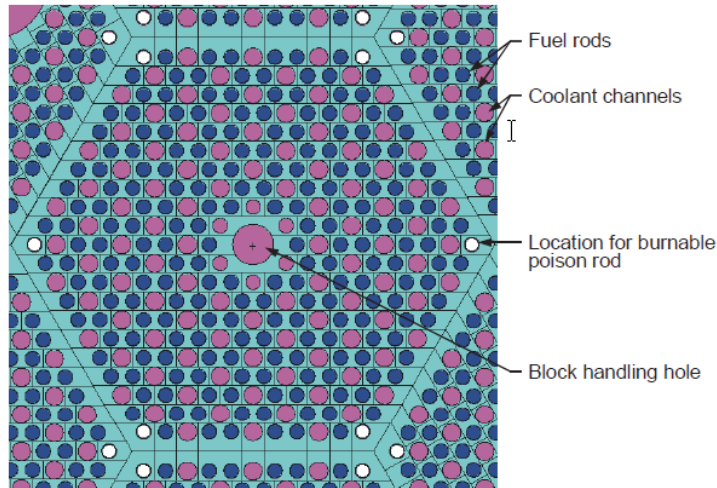
Figure 1. Lattice physics representation of a fuel block model.
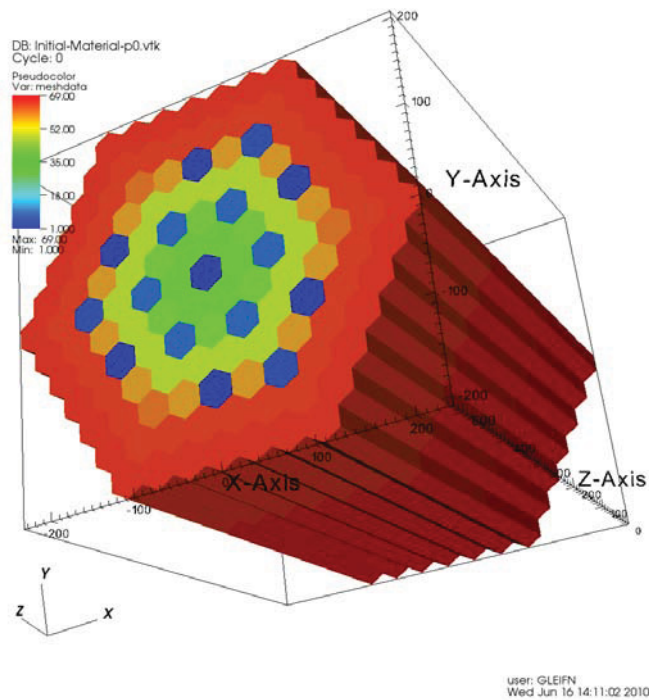
Figure 2. Representation of the whole core physics model.

The generation of cross-sections for annular HTRs is an active area of research. Previous studies [3,7,8,9] have shown that the neutronic characteristics of these cores complicate this essential step in the calculation process. This work attempts to address some of the areas previously identified as problematic, but significant challenges still remain. These challenges are further discussed in the cross-section generation section.

2

2.   PURPOSE

As initially discussed, the V&V task is essential in determining the applicability and predictive capability of computer codes for a particular reactor designs. The purpose of this report is to commence the V&V of selected codes for use in the analysis of the NGNP prismatic design. The two neutronic codes evaluated for the analysis of the prismatic NGNP at INL are the DRAGON 4 transport and cross-section preparation code and the HEXPEDITE whole-core neutron-diffusion solver.

The specific goals of this report are: (1) the further verification multiplication factor calculation in HEXPEDITE, (2) the validation of the DRAGON 4-HEXPEDITE methods in the calculation of the core multiplication factor and multiplication factor-based parameters, (3) the identification of gaps in the current cross-section generation and calculation capabilities, and (4) provide some recommendations.

Previous work on the HEXPEDITE methodology [11,12,13] has tested the approach against other spatial discretizations for the neutron diffusion equation in hexagonal and triangular geometry, such as the nodal expansion method (NEM) and finite difference method (FDM). These studies have established HEXPEDITE's superiority in terms of accuracy and runtime over NEM and FDM. To further verify the multiplication factor calculation in HEXPEDITE, a comparison to a reference solution from the INL's INSTANT transport solver using the same cross-section set is conducted. The INSTANT calculations are performed with a P1 solution method to provide a more consistent comparison to the HEXPEDITE nodal diffusion method.

A second verification approach with SERPENT is attempted, but this code is still under its early stages of testing at the INL. Strictly speaking, this is not a classic verification, since the HEXPEDITE code solves the diffusion equation, whereas SERPENT solves the linearized Boltzmann transport equation. Nevertheless, the comparison should show how well the diffusion theory based solution in HEXPEDITE approximates the transport theory solution. The great advantage of the SERPENT code is its capability to generate diffusion-theory parameters including diffusion coefficients and a full scattering matrix from a high-fidelity Monte Carlo calculation. This dataset can be subsequently input into the HEXPEDITE code to generate the diffusion solution for the comparison.

The validation of the DRAGON 4 and HEXPEDITE methods involves the calculation of the following multiplication factor and multiplication factor-based parameters for the HTTR core:

1.   19-column annular core critical configuration at 300 K

2.   30-column (full core) critical configuration at 300 K

3.   30-column (full core) isothermal temperature coefficients of reactivity.

The first two calculations provide a measure of the accuracy of the multiplication factor computation. The calculation of the isothermal coefficients of reactivity also includes initial validation of the temperature dependence of the fine-group cross-sections and temperature interpolation models within DRAGON 4.

3. HTTR REACTOR DESCRIPTION

3.1 General Description

The HTTR specifications and descriptions included in Section 3 have been directly adopted from the IRPhE project reports [5,6]. Detailed information and reference documentation can be found in the original reports. The HTTR is a 30-MWth helium-cooled, graphite-moderated reactor located at the Oarai Research and Development Center in Japan and currently operated by the Japan Atomic Energy Agency's (JAEA). This facility was constructed with the objective to establish and upgrade the technological basis for advanced high temperature gas-cooled reactors (HTGRs) as well as to conduct various irradiation tests for innovative high-temperature research. The core size of the HTTR represents about one-half of the core size of future HTGRs, and the high excess reactivity of the HTTR, necessary for compensation of temperature, xenon, and burnup effects during power operations, is similar to that of future HTGRs. During the start-up core physics tests of the HTTR, various annular cores were formed to provide experimental data for verification of design codes for future HTGRs. The major design specifications are included in Table 1.

Table 1. Major design specifications of the HTTR.

Thermal Power	30 MW
Outlet Coolant Temperature	850-950°C
Inlet Coolant Temperature	395°C
Primary Coolant Pressure	4 MPa
Core Structure	Graphite
Equivalent Core Diameter	2.3 m
Effective Core Height	2.9 m
Average Power Density	2.5 W/cm^3
Fuel	UO_2
Enrichment	3 to 10 wt%
	6 wt% (average)
Type	Pin-in-Block Type
	Coated Fuel Particles
Burnup Period (effective full power days [EFPD])	660 days
Block Material	Graphite Block
Coolant Material	Helium Gas
Flow of Direction in Core	Downward
Reflector Thickness	
Top	1.16 m
Side	0.99 m
Bottom	1.16 m
Number of Fuel Blocks	150
Number of Fuel Columns	30
Number of Pairs of Control Rods	
In Core	7
In Reflector	9

The active core has a height of 290 cm and effective diameter of 230 cm (Figure 3 and Figure 4). The core consists of hexagonal graphite blocks 580-mm high and 360-mm across flats. These fuel blocks, control rod (CR) guide blocks, replaceable reflector blocks, and irradiation blocks are stacked vertically into columns. The active core contains 30 fuel columns. One column contains five stacked fuel blocks. Each fuel block has 31 or 33 coolant channels, into which fuel rods are inserted. Fuel rods consist of a graphite sleeve containing 14 fuel compacts. Each fuel compact contains about 13,000 coated fuel particles (CFPs) randomly embedded in a graphite matrix. Fuel-block assembly is depicted in Figure 5. A CFP is comprised of a spherical fuel kernel of low-enriched UO_2 with a coating of four layers. The core has 12 different uranium enrichments between 3.4 and 9.9 wt% (as shown in Table 2) to reduce the maximum fuel temperature and increase the outlet temperature of the gas. Fuel blocks of more highly enriched uranium are placed in the upper- and outer-core regions. Burnable poisons (BPs), made of boron carbide and carbon, are inserted into two of three holes below the dowel pins in the fuel blocks. The coolant gas flow is downward through annular channels between the graphite blocks and fuel rods. Sixteen pairs of CRs are used for reactivity control. A pair of CRs is individually moved by a CR driving mechanism located in standpipes above the core. The CRs are inserted into two of three channels in the CR guide columns.

The position of blocks in the core is described by a vertical position number and column number. The vertical number range from 1 through 9, where the top of the blocks is the first layer, and the bottom of the blocks is the ninth layer. The column number is named according to Figure 6. An example is position 4C05, which is the fourth block from the top, the second ring of fuel from the center of the core, and the fifth block from the north in clockwise direction. All 30 fuel columns are grouped concentrically into four fuel zones.

The core consists of vertical columns of hexagonal blocks arranged on a uniform triangular pitch. The triangular pitch of the columns on each support block is 36.2 cm at cold conditions. The effective diameter of the core, including removable reflectors, is 3.258 m. The overall dimensions of the primary components of the core, including permanent reflectors, are a diameter of 4.25 m and a height of 5.25 m.

Figure 3. Vertical cross-section of the HTTR.
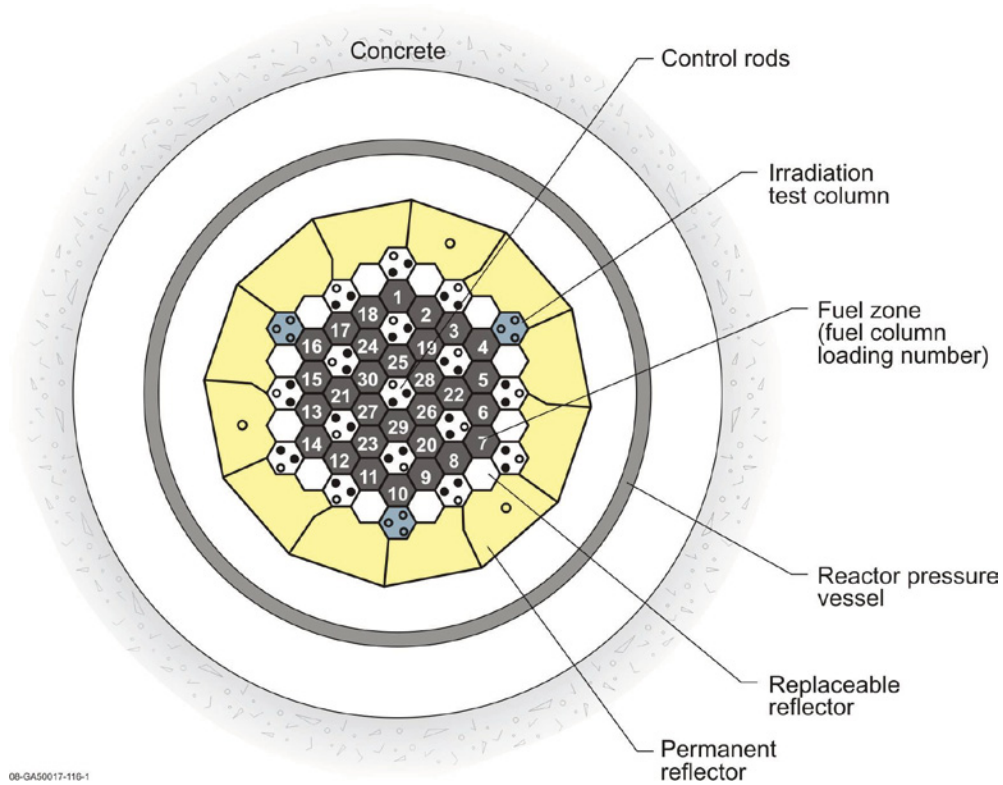
Figure 4. Horizontal cross-section of the HTTR.
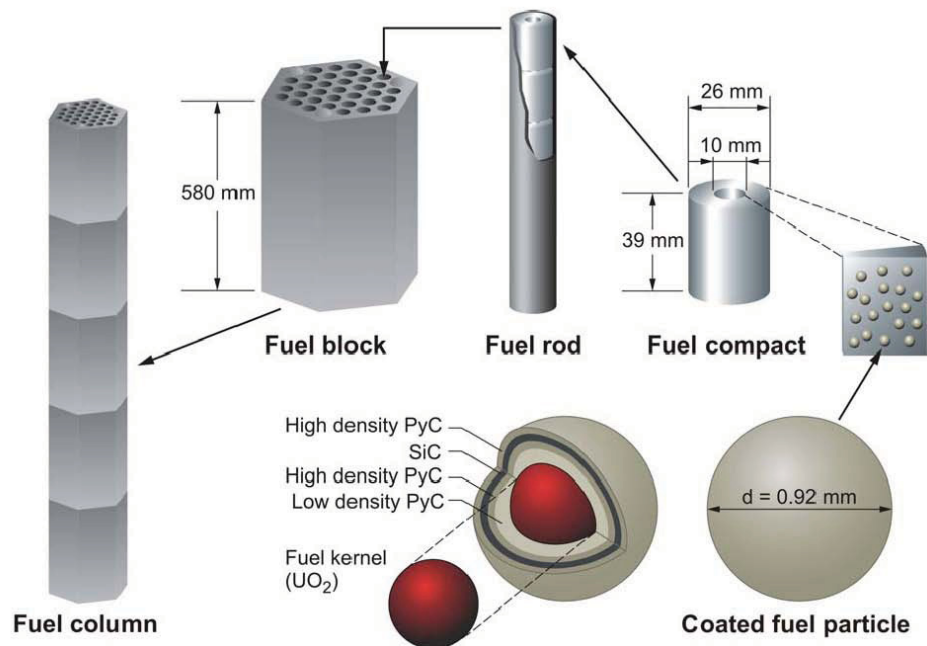
Figure 5. HTTR fuel kernel to fuel column schematic.

Table 2. Uranium enrichments of the HTTR core.

Layer[c]	Fuel Zone Number[a]				
	1	2	3	4	BP[b]
1	6.7	7.9	9.4	9.9	2.0
2	5.2	6.3	7.2	7.9	2.5
3	4.3	5.2	5.9	6.3	2.5
4	3.4	3.9	4.3	4.8	2.0
5	3.4	3.9	4.3	4.8	2.0

(a) (U_{235}) enrichment (wt%).

(b) Nat-B concentration (wt%).

(c) Layer number from top fuel block.
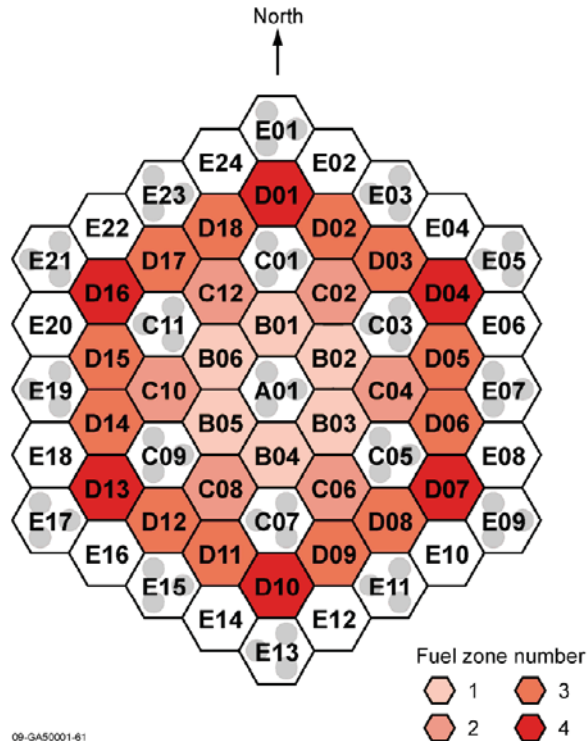
Figure 6. Fuel column name and zone number in the HTTR core (Bess report).

3.2 Prismatic Reactor Fuel

The fuel element of the HTTR is a so-called pin-in-block type fuel element, which is composed of fuel rods in a hexagonal graphite block. A fuel assembly consists of fuel rods, two BP rods, and a fuel graphite block. Each fuel rod (Figure 5) comprises a graphite sleeve with 14 fuel compacts containing CFPs. The fuel rods are inserted into vertical channels of 41-mm diameter in the fuel graphite block to form annular coolant channels between the holes and rods. There are two types of fuel graphite blocks: 31- and 33-holed. There are twelve different uranium enrichments in the core (Figure 7 and

Table 2). The enrichment of all compacts in a fuel assembly does not vary. The fuel assembly is classified by the uranium enrichment, number of fuel rods, and the type of BPs.

The core was divided axially into five layers to allow for optimization of the axial power distribution. A layer corresponds to a fuel block. The same uranium enrichments were loaded into the fourth and fifth layers because the power density decreases due to neutron leakage to the bottom reflector. It corresponds to the tail of the exponential form. Therefore, the axial power distribution was optimized by decreasing the uranium enrichment ratios from the first layer to the fourth. The radial power distribution was optimized by adjusting the uranium enrichments so that the maximum radial power peaking in each fuel column could be brought close to unity. The uranium enrichment was increased from the core's center to the periphery to compensate for the decrease in the power production caused by neutron leakage into the side reflector.

The fuel blocks were to be completely replaced by fresh fuel blocks after each burn-up cycle. Each fuel element in the core will be discharged every three years. The fuel elements keep their original position during their lifetime in the core. However, the HTTR has not been refueled for at least the first 10 years of its operation.
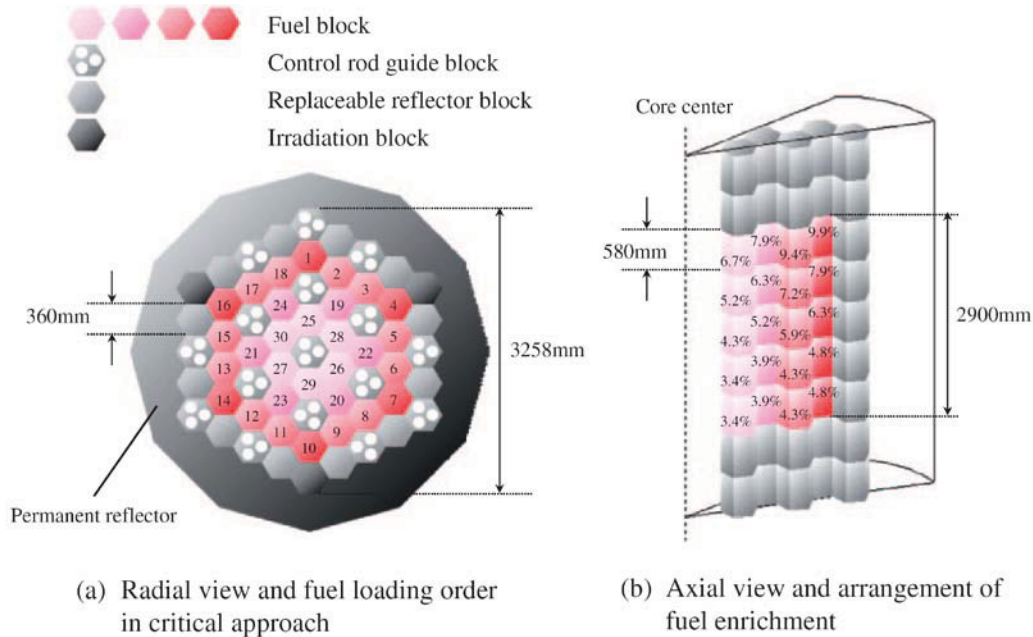
Figure 7. Uranium enrichments of the HTTR core.

There are four types of HTTR fuel. The A-type fuel is the primary driver fuel for the HTTR. B-type fuel rods, namely B-1, B-2, and B-3, have different coating-layer specifications for the CFPs and are used in irradiation tests of advanced fuels. Fuel specifications are in Table 3. The A-type fuel is currently the only fuel in use, as the B-type fuel has yet to be fabricated. Specifications for the fuel assemblies are compiled in Table 4.

A CFP consists of a spherical fuel kernel of low enriched UO_2 (600-μm diameter at 95% theoretical density [TD]) with a tri-isotropic (TRISO) coating: low-density, porous pyrolytic carbon (PyC) buffer layer (60 μm), high-density inner isotropic PyC layer (30 μm), a SiC layer (25 μm), and a final outer pyrolytic carbon (OPyC) layer (45 μm), as shown in Figure 5 and Table 3. The CFPs are embedded in graphite matrix of the fuel compact. The fuel compact is a hollow cylinder with 10-mm inner diameter, 26-mm outer diameter, and a 39-mm height.

Table 3. Specification of CFPs. A-type fuel is the primary fuel for the HTTR with B-type fuel representing advanced fuel for irradiation tests.

	A-Type	B-1/B-2 Type	B-3 Type
Fuel Type	Rod	Rod	Rod
Fuel Coating Type	TRISO	TRISO	TRISO
Diameter of Particle (μm)	920	940	830
Fuel Kernel			
Material	UO_2	UO_2	$(U,Th)O_2$ (Th/U=4)
Density (% of TD)	95	95	95
Diameter (μm)	600	570	500
Materials and Thickness (μm) of Coatings			
1st Layer	Low-density PyC 60	Low-density PyC 80	Low-density PyC 60
2nd Layer	High-density PyC 30	High-density PyC 30	High-density PyC 30
3rd Layer	SiC 25	SiC(B-1)/ZrC(B-2) 35	SiC 30
4th Layer	High-density PyC 45	High-density PyC 40	High-density PyC 45
Enrichment of (U_{235})(wt.%)	3-10 (Ave. 6)	5	20
	A-Type	B-1/B-2 Type	B-3 Type
Fuel Type	Rod	Rod	Rod
Fuel Coating Type	TRISO	TRISO	TRISO
Diameter of Particle (μm)	920	940	830

Table 4. Main specifications of HTTR fuel.

Fuel Kernel:	
Material	UO_2
Diameter (μm)	600
Density (g/cm^3)	10.41[a]
Coated Fuel Particle:	
Type/Material	TRISO
Diameter (μm)	920
Impurity (ppm)	<3 (Boron Equivalent)
Fuel Compact:	
Type	Hollow Cylinder
Material	CFPs, Binder, and Graphite
Outer/Inner Diameter (cm)	2.6 / 1.0
Length (cm)	3.9
Packing Fraction of CFPs (vol.%)	30 (A and B-3)
	35 (B-1 and B-2)
Density of Graphite Matrix (g/cm^3)	1.7
Impurity in Graphite Matrix (ppm)	<1.2 (Boron Equivalent)
Fuel Rod:	
Outer Diameter (cm)	3.4
Sleeve Thickness (mm)	3.75
Length (cm)	54.6
Number of Fuel Compacts	14
Number of Rods in a Block	31/33
Graphite Sleeve:	
Type	Cylinder
Material	IG-110 Graphite
Impurity (ppm)	<1 (Boron Equivalent)
Length (cm)	58
Gap Width between Compact and Sleeve (mm)	0.25
Graphite Block:	
Type/Configuration	Pin-in-Block/Hexagonal
Material	IG-110 graphite
Width across Flats (cm)	36
Height (cm)	58
Fuel Hole Diameter (cm)	4.1
Density (g/cm^3)	1.75
Impurity (ppm)	<1 (Boron Equivalent)

The porous PyC coating layer, called the buffer layer, attenuates fission recoils and provides void volume for gaseous fission products and carbon monoxide. The inner pyrolytic carbon (IPyC) coating layer acts as a containment for the gases. The silicon carbide (SiC) coating layer provides mechanical strength for the particle and acts as a diffusion barrier to metallic fission products that diffuse easily through the IPyC layer. The OPyC coating layer protects the SiC coating layer mechanically.

With about 13,000 fuel particles defined for each fuel compact, the corresponding packing density is about 30%. The sintered fuel compacts are contained in a fuel rod that is 34 mm in outer diameter and 577 mm in length. The form of the fuel rod (graphite sleeve containing 14 fuel compacts) is shown in Figure 8. The annular fuel pin has an inner diameter of 26.25 mm. The helium gas flows downward through the 3.5-mm annular gap between the hole and the fuel rod.
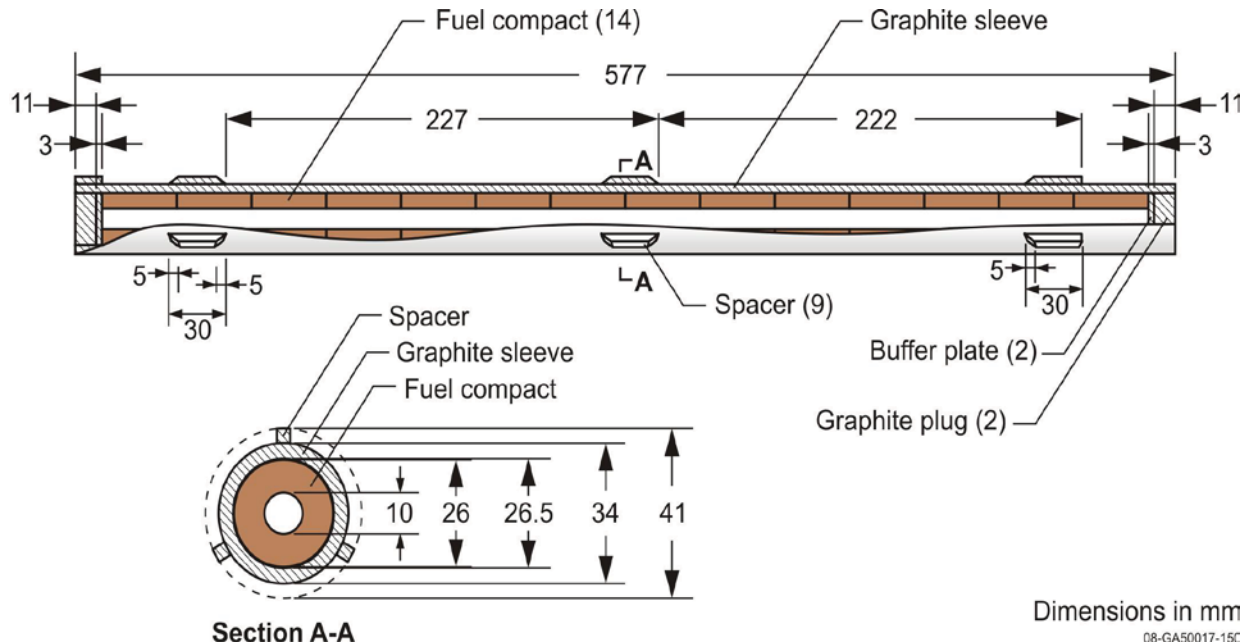
Figure 8. HTTR fuel rod.

The graphite block is a prismatic hexagonal block with a 580-mm height and 360-mm across the flats. Blocks in Fuel Zones 1 and 2 have 33 fuel holes, and blocks in Fuel Zones 3 and 4 have 31 fuel zones. The form of the block is given in Figure 9 and Figure 10, respectively.

Three threaded dowels are installed on the top face of the fuel blocks that are coupled with sockets in the bottom face of the block located above it. A hole at the center of each fuel block is provided for fuel handling. The hole profile is shaped so that a lifting ledge is machined at the lower end. The grapple head of the fuel-handling machine stands against this ledge when lifting the block. Additional holes are provided in the corners of the blocks for the insertion of the BP rods. The arrangement pattern of the fuel blocks in the core is shown in Figure 11. There is a slight key slot in the holes of the fuel blocks to align and hold in the fuel rods.

Figure 9. Fuel block for 33-pin fuel assembly. Dxx represents the diameter in xx (mm).

51.5

54.5

51.5

54.5

360

Fuel hole | Fuel handling hole | BP insertion hole

D50

90

D41

D30

60

D15

D45

100

580

Dimensions in mm

08-GA50017-151-3
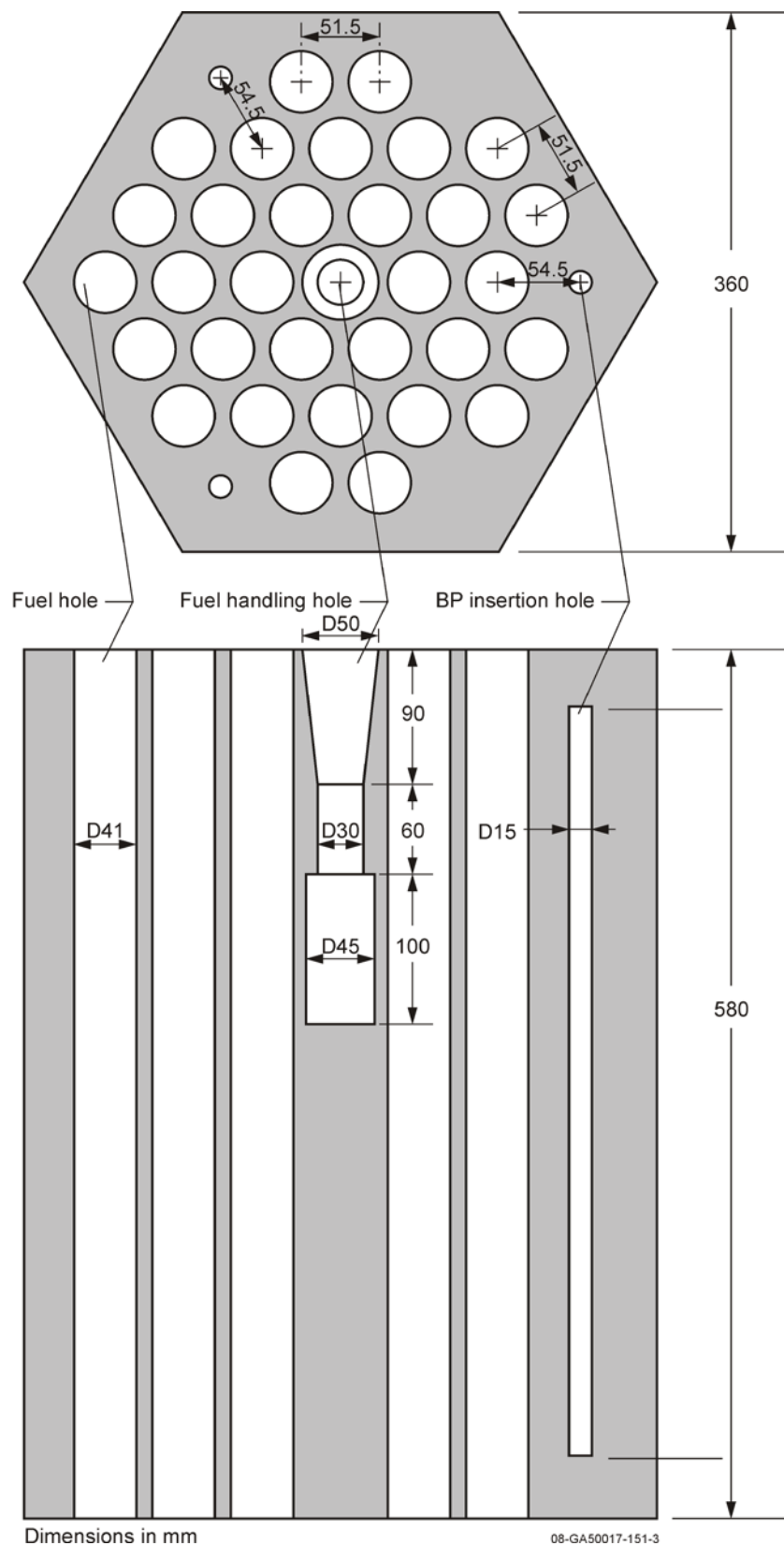
Figure 10. Fuel block for 31-pin fuel assembly. Dxx represents the diameter in xx (mm).
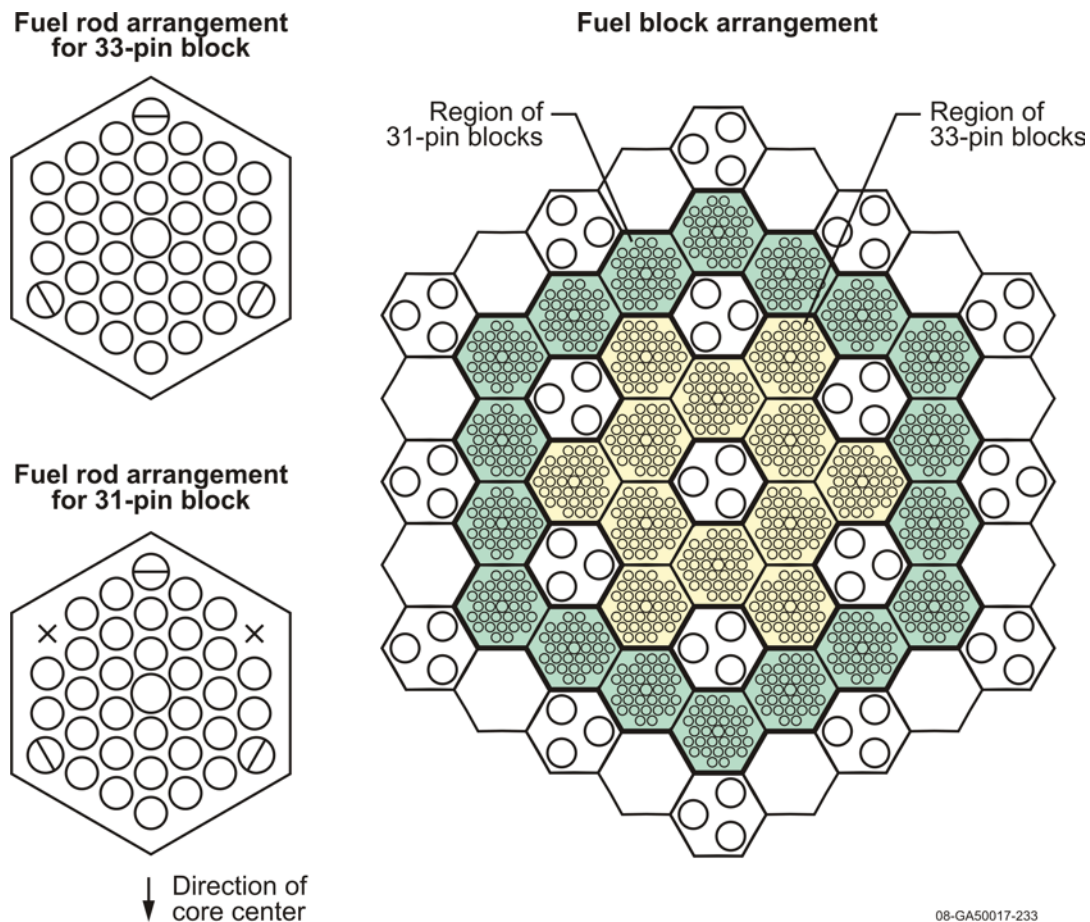
Figure 11. Core Arrangement Plan of Fuel Blocks with 33 and 31 fuel rods.

3.2.1 Burnable Poisons

BP rods are inserted into two of the three BP insertion holes in the fuel graphite blocks (Figure 9 and Figure 10). The BP insertion holes are under the 3 dowel pins of the fuel graphite block and are 15 mm in diameter and 500 mm long. One hole is empty, without the BP rod. The BP rod has a diameter of 14 mm. The rod contains BP pellets and graphite disks, as shown in Figure 12. The graphite disks are placed between the BP pellets. The BP cylindrical pellets are each 20 mm in height.

The large initial excess reactivity from fresh fuel is counteracted through the use of BPs. Optimization of the specifications for the BPs reduces deviation from the optimum power distribution due to burnup effects. This is done by changing the poison atom density and radius throughout the core. It then becomes possible to operate the reactor during full power operation at 950°C without changing the insertion position of the control rods.

15
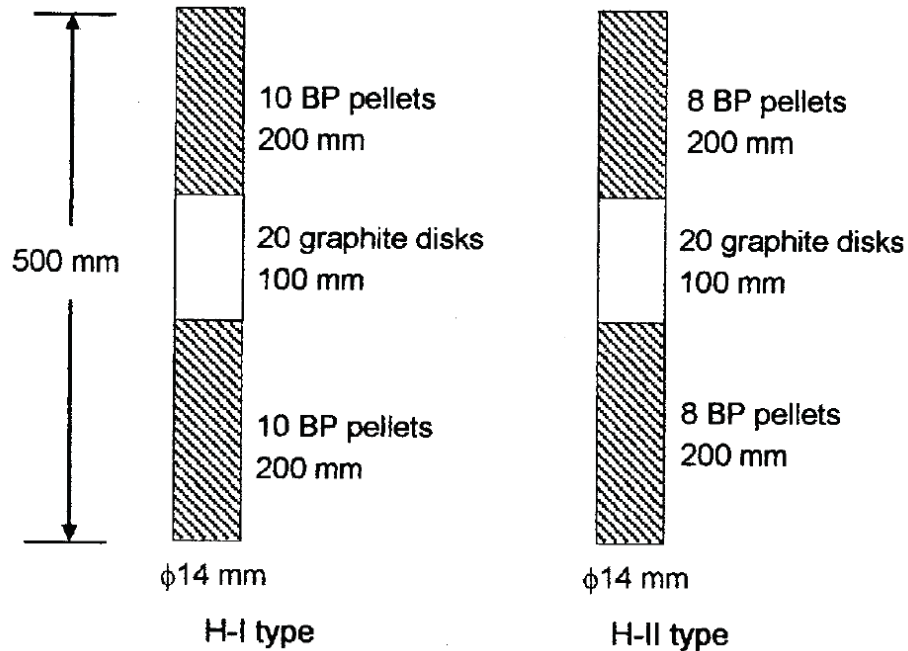
Figure 12. Configuration of BP pellets and graphite disks in a BP rod.

3.3 Control Rods and Reserve Shutdown System

Toshiba and Ishikawajima-Harima Heavy Industries led development of the reactivity control instrumentation: the control rod drive mechanism and the reserve shutdown system.

There are 16 pairs of CRs: seven in the fuel region and nine in the replaceable reflector region. They are inserted into the holes of the CR guide columns. The control rod guide blocks have three holes: two for control rod insertion and one for the emergency reserve shutdown system (RSS). Figure 14 shows the position of the CR insertion holes and RSS holes in the core and replaceable reflector.

The center CR can be removed such that the center column of the core could be used for an irradiation test. The CR system can achieve subcriticality from any operation state and maintain subcriticality in the cold core even when a pair of CRs sticks into an operational position. In case of a scram during normal operations, the CRs in the replaceable reflector region are inserted at first, and the rest of the CRs are inserted after the core has cooled down. This prevents the control rod cladding from being exposed to temperatures above 900°C. A pair of CRs is driven by one drive mechanism and released from the mechanism to be inserted by gravity in the event of a reactor scram. A pair of CRs is individually moved by a control rod drive mechanism located in stand pipes connected to the hemispherical top head closure of the reactor pressure vessel.

The control rods were designed to provide a shutdown margin of more than 0.01 $\Delta k/k$, even when one pair of rods with the maximum reactivity worth is completely withdrawn and cannot be inserted. The reserve shutdown system also is designed to provide more than 0.01 $\Delta k/k$, even when the CR system is unavailable. The maximum reactivity addition rate is limited to CR withdrawal of less than 50 mm per step and a reactivity addition rate limit of 2.4×10^{-4} $\Delta k/k$-s. The maximum driving speed of the CR is 60 cm/min.

Each CR consists of 10 neutron absorber sections connected with metallic spines and support rings (Figure 13). Each section contains five sintered compacts of B_4C and C as neutron absorbers in the annular space. The CR pairs were named center (C), Ring 1 (R1), Ring 2 (R2), and Ring 3 (R3) from the

16

center to the outside, as shown in Figure 14. Both R2 and R3 CRs are in the replaceable reflector region surrounding the core, where the six CR pairs on the sides of the hexagonal loading pattern are R2 CRs and the three remaining CR pairs at corners of the hex are R3 CRs. The CR positions at critical conditions were measured to evaluate the calculation accuracy. They were inserted from top to bottom. The bottoms of the inserted CRs were kept almost at the same level at critical conditions. The CR positions were defined with distance from the bottom of the fifth fuel layer. The R3 CRs were fully withdrawn at critical conditions.
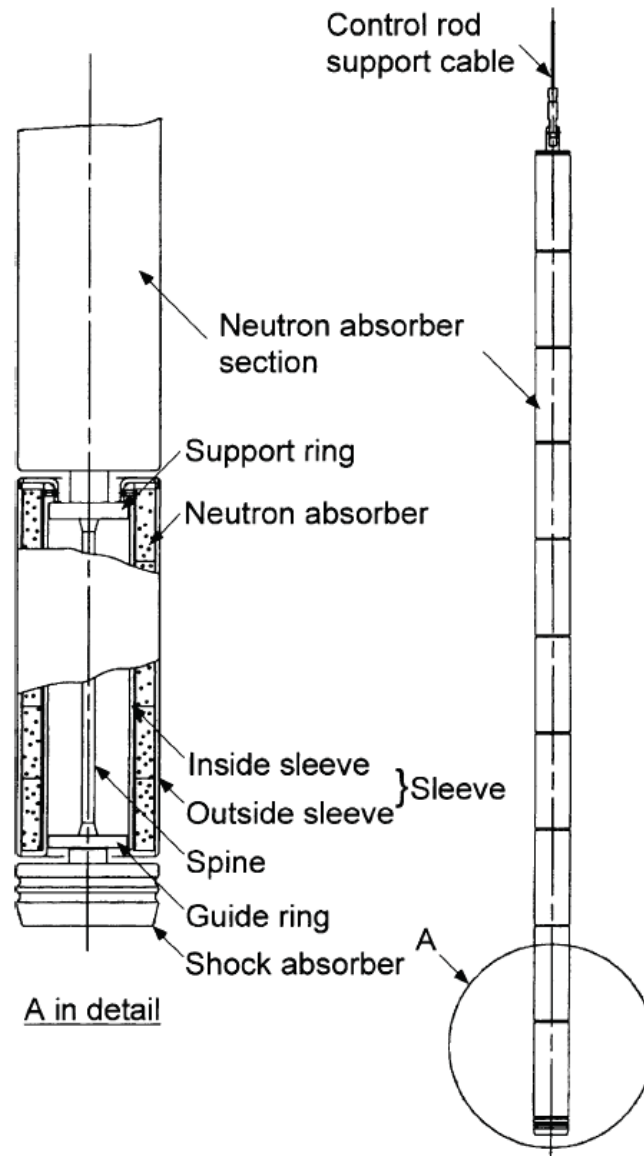
Figure 13. Control rod of HTTR.
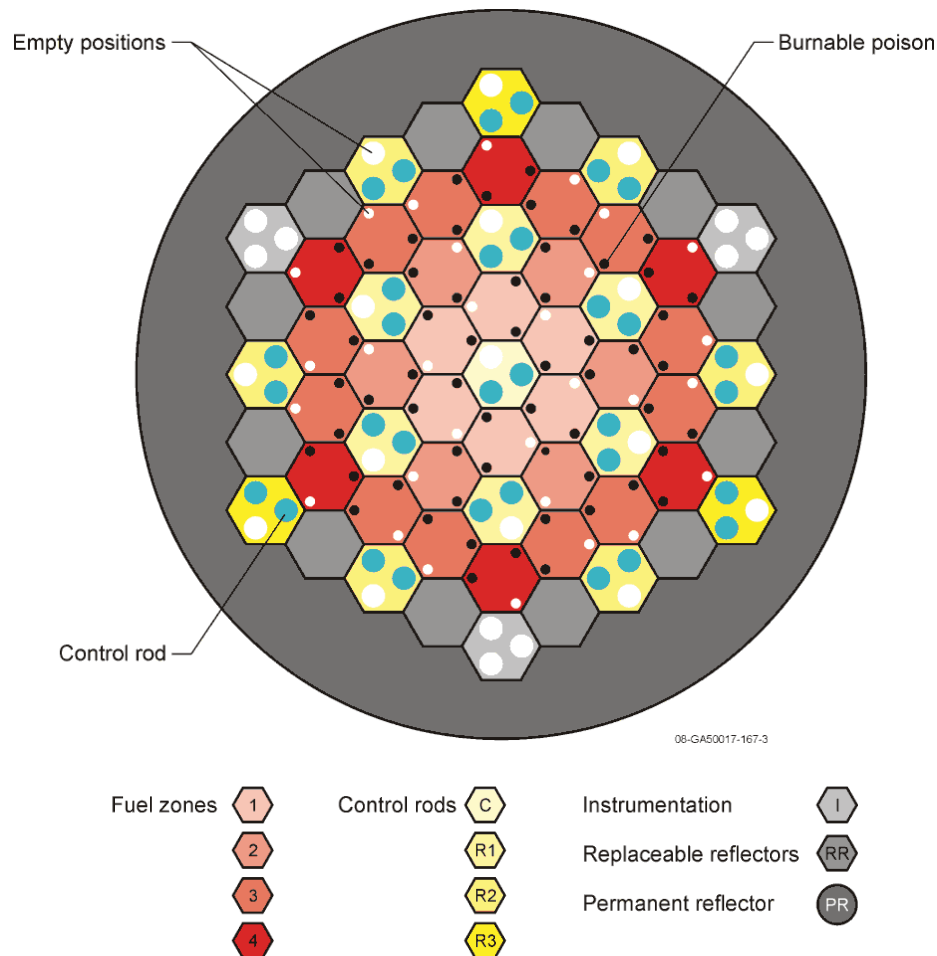
Figure 14. Control rod map.

To reduce thermal stresses in the sleeves, the neutron absorber sections and spine are separated from each other, and each section is sustained by a support ring. The absorber section is assembled from parts with gaps between them, and all parts are mechanically connected without welds. Each absorber section contains a guide ring to restrain it from rolling too much. The lower end of the spine is attached to a tubular shock absorber. At the bottom of the core are graphite dishes, also called shock absorbers, which absorb the impact of a CR. The annular space of each absorber section contains the sintered compacts with a density of 1.9 g/cm^3.

The total height of the CRs is 3094 mm. The pellets are surrounded by a 3.5-mm thick sleeve of Alloy 800H. Inner and outer diameters of the CRs are 65 and 113 mm, respectively. The height of the pellet stack in a single absorber section is 29 cm. The CR and RSS specifications are included in Table 5.

The RSS absorbers are a system of pellets produced by sintering B_4C powder and graphite. These pellets can be released from the storage hoppers into holes in the CR guide columns to act as a backup system for the CR system. In an accident when the CRs cannot be inserted, an electric plug is pulled out by a drive motor, and the neutron-absorbing pellets falls into the core by gravity.

CR guide blocks have the same envelope dimensions as the fuel blocks and use the same dowel/socket connections. The CR and RSS insertion holes have a diameter of 123 mm. The bottom block of the CR guide column contains B_4C/C pins for thermal neutron shield. Specifications for CR blocks are found in Figure 15 and Table 6.

Table 5. Specifications of the CR system and the RSS.

CR System:	
Type	Double Cylinders with Lid and Vent
Number	16 Pairs (32 Rods)
	15 Pairs when Irradiation Test is in Center Column
Total Length (m)	3.1
Outer Diameter (mm)	113
Inner Diameter (mm)	65
Sleeve	
Thickness (mm)	3.5[a]
Material	Alloy 800H
Neutron Absorber	
Density (g/cm^3)	1.9
Outer Diameter (mm)	105[b]
Inner Diameter (mm)	75
Material	Sintered Compact of B_4C/C
Natural Boron Concentration (wt%)	30
Spine	
Diameter (mm)	10
Material	Alloy 800H
RSS:	
Drive Mechanism	Drop B_4C/C Pellets by Gravity
Number	16
Effective Length (m)	3.1
Hole	
Packing Fraction (vol%)	55
B_4C/C Graphite Pellets	
Density (g/cm^3)	1.9
Diameter (mm)	13
Length (mm)	13
Material	Sintered Compact of B_4C/C
Natural Boron Concentration (wt%)	30

(a) Mathematically, the clad thickness does not match up with the other dimensions provided for the control rod. It is unclear whether gaps exist between absorber and clad material or the cladding is thicker.

(b) Reference 4 lists this value as 115, which cannot fit within the designated cladding dimension. All other values reported in Reference 4 match values in Reference 7.
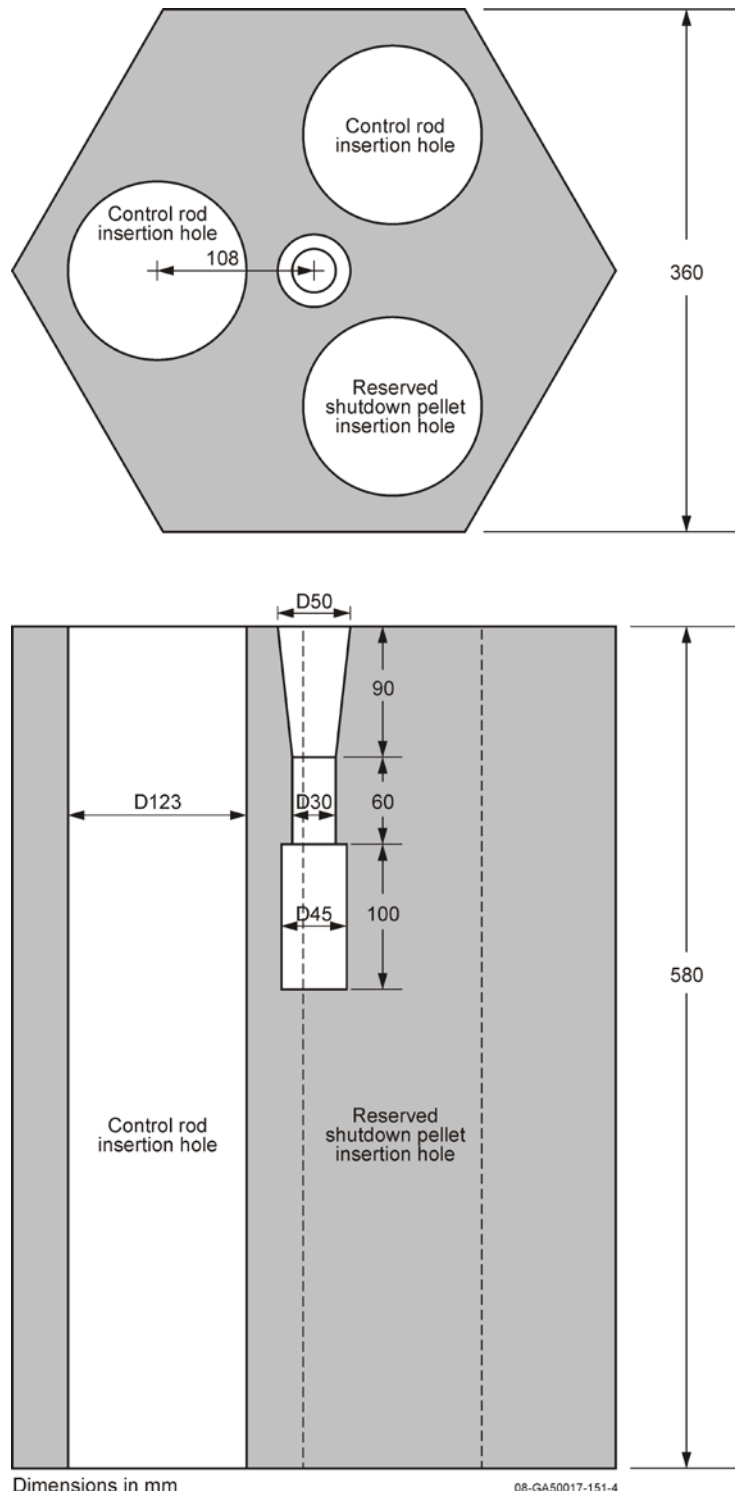
Figure 15. CR guide block. Dxx represents the diameter in xx (mm).

Table 6. Specifications of reflector blocks and CR guide blocks.

Replaceable Reflector Blocks	
Material	IG-110 graphite
Width across Flats (cm)	36
Height (cm)	58
Density (g/cm^3)	1.75
Impurity (ppm)	<1 (boron equivalent)
Control Rod Guide Blocks	
Material	IG-110 graphite
Width across Flats (cm)	36
Height (cm)	58
Density (g/cm^3)	1.75
Impurity (ppm)	<1 (boron equivalent)
Hole	
Diameter (cm)	12.3
Number	3
Permanent Reflector	
Material	PGX graphite
Density (g/cm^3)	1.73
Impurity (ppm)	<5 (boron equivalent)

The top of the control rod guide columns and irradiation columns are 100 mm lower than that of the fuel columns because the ninth-layer blocks of these columns are 480 mm in height. Each horizontal gap width between two columns is 2 mm on average.

When the CRs are fully inserted, the lower ends of all CRs are on the same plane with the bottom face of the seventh layer of the fuel column. When the CRs are fully withdrawn, their upper limit is the upper face of the first replaceable reflector block over the fuel region with exception of the R2 CRs, which have upper limits at 725 mm below the top of the first block. Axial CR positions are shown in Figure 16.

The fully withdrawn positions of R2 were different from those of C, R1, and R3; they are limited because the R2 rods were used for scrams at full-power operation. The C and R1 CRs would then be inserted into the core only after core temperatures decreased to maintain shutdown.
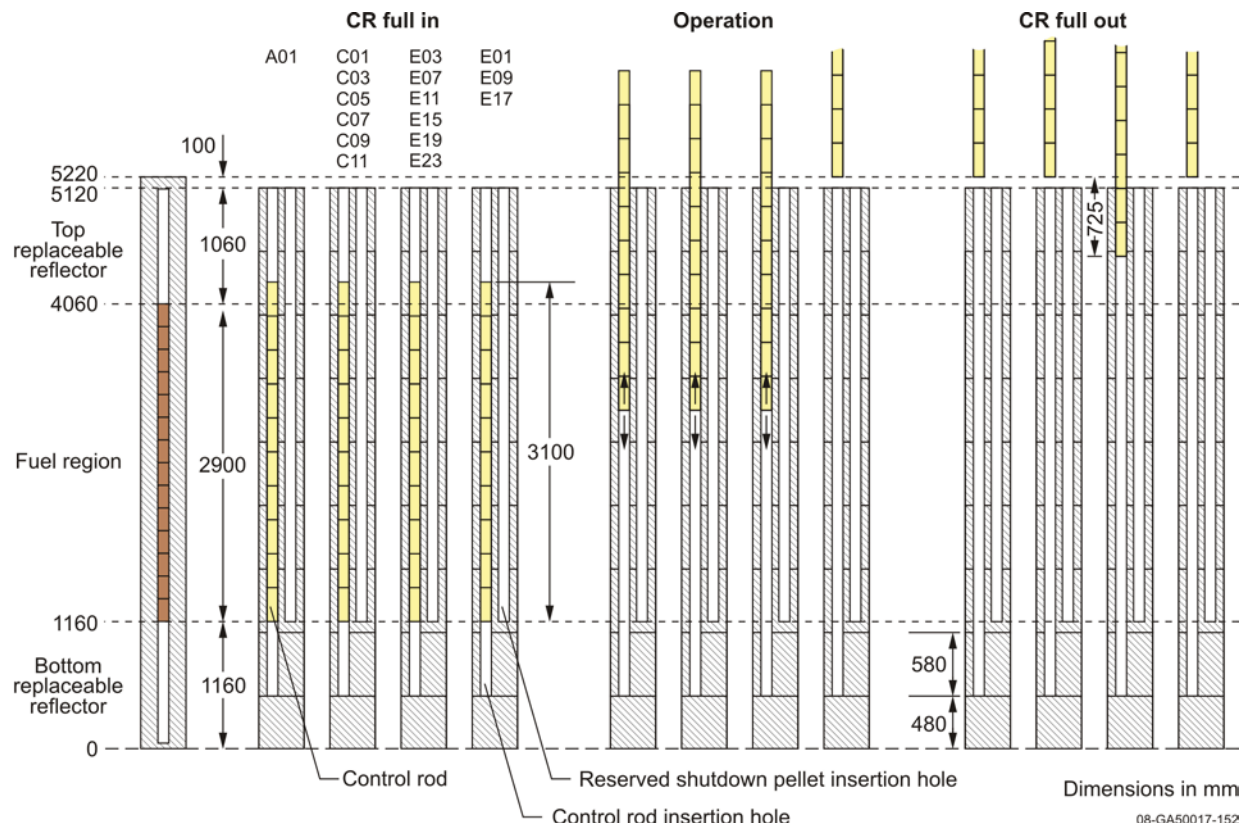
Figure 16. Axial CR positions.

3.4   Graphite Blocks

The five fuel assembly blocks within a fuel column have two top reflector blocks and two bottom reflector blocks.

The top and bottom replaceable reflector blocks have the same basic configuration as the fuel blocks but do not contain fuel rods. These reflector blocks, above and below the active core, have the same arrangement of coolant channels as the fuel blocks within the same columns. The bottom replaceable reflector block below each fuel block column provides a transition of the many coolant channels to a single large channel, which mates with the coolant channels within the hot plenum blocks. The alignment of the fuel, CR guide, and replaceable reflector columns with the hot plenum blocks is maintained by dowel/socket connections in the bottom reflector blocks, which fit into the hot plenum blocks. The bottom layer of reflector blocks contains B_4C/C pins for the thermal neutron shield.

The arrangement of coolant channels (with 23-mm inner diameter) in the top replaceable reflector blocks corresponds to that of coolant channels (with 41-mm inner diameter) in the fuel assemblies within the same column. The upper bottom replaceable reflector block (eighth layer) has the same arrangement of coolant channels as the top replaceable reflector block. The lower bottom reflector block (ninth layer) has six large coolant channels.

All blocks except the bottom block of the CR guide column and the irradiation column are 58 cm in height and 36 cm in width across flats. Boron pins are installed into the lower parts of blocks in the ninth layer for neutron shielding.

22

3.5   Dummy Blocks

Before fuel loading, the whole fuel region in the core was filled with graphite dummy blocks. There are two types of dummy blocks: graphite blocks with three large holes and those with three small holes. The graphite blocks with three large holes were used as CR guide columns for out-pile seismic tests of the core structure. The others with three small holes were newly produced as dummy fuel blocks.

The external form of the dummy fuel block is the same as that of a fuel graphite block.

3.6   Replaceable Reflectors

Twelve replaceable reflector columns are adjacent to the active core region and surrounded by permanent reflector blocks.

The side replaceable reflector blocks adjacent to the core have the same envelope dimensions as fuel blocks but are solid graphite and contain only a central handling hole for removal and insertion (Figure 17).

The replaceable reflector blocks, located at the top and the bottom fuel columns, are shown in Figure 18 and Figure 19 for the 33-pin and 31-pin fuel assemblies, respectively. The replaceable reflector blocks have the same regular hexagonal shape and pitch as described for the fuel blocks.

3.7   Permanent Reflectors

A permanent graphite reflector region surrounds the core and holds it together (Figure 4). The 12 permanent reflector blocks are in the form of a large polygonal graphite block 4250 mm across flats. The permanent reflector blocks have holes for irradiation tests and neutron detectors, giving a void fraction of approximately 0.7%.

The permanent reflector is an assembly of 12 circumferential segments in 8 axial layers.

The total height of the permanent reflectors is about 8 m. Each circumferential segment is keyed on the adjacent surface and bound to the core restraint mechanism. By-pass flow of the coolant is restricted between adjacent blocks by face contact and seal elements.
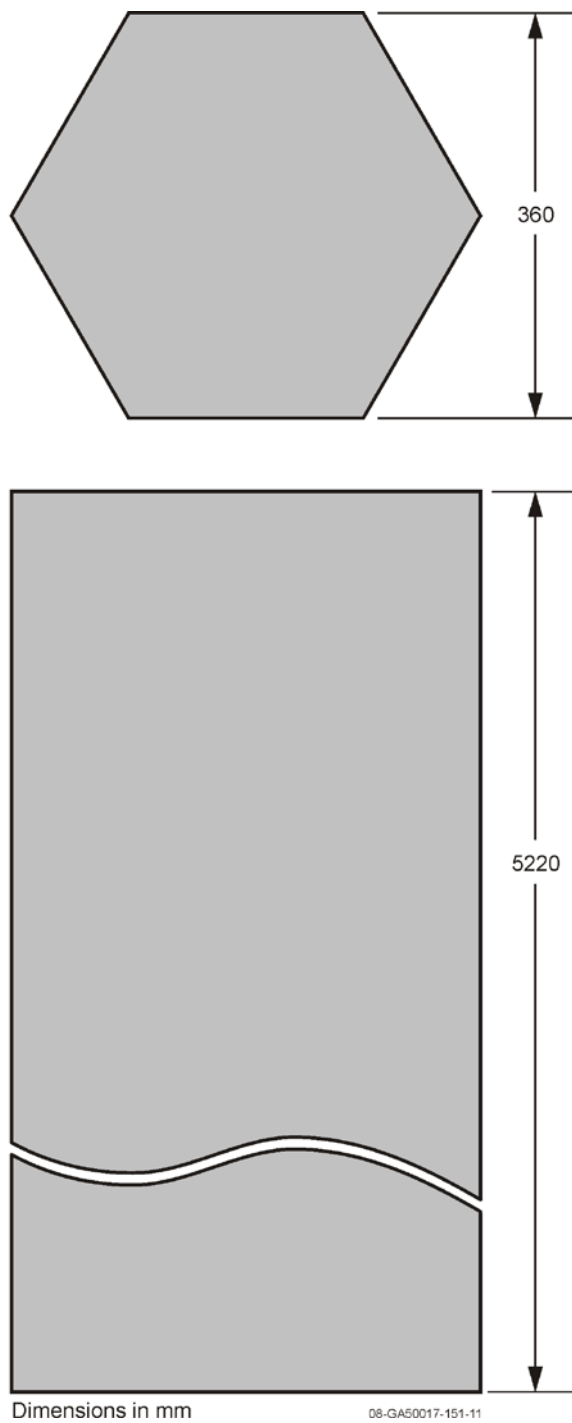
Figure 17. Replaceable reflector column.
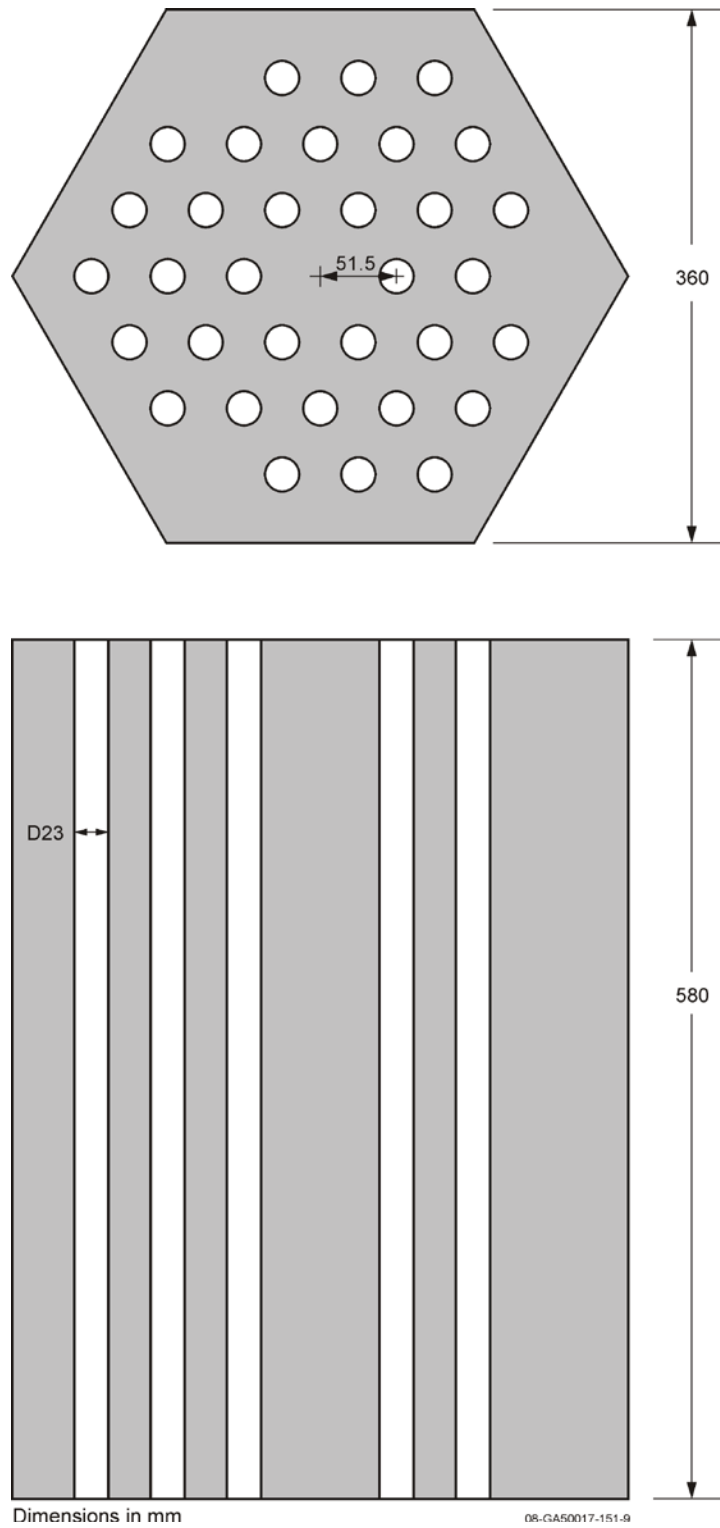
Figure 18. Replaceable reflector block for 33-pin fuel assembly. Dxx represents the diameter in xx (mm).
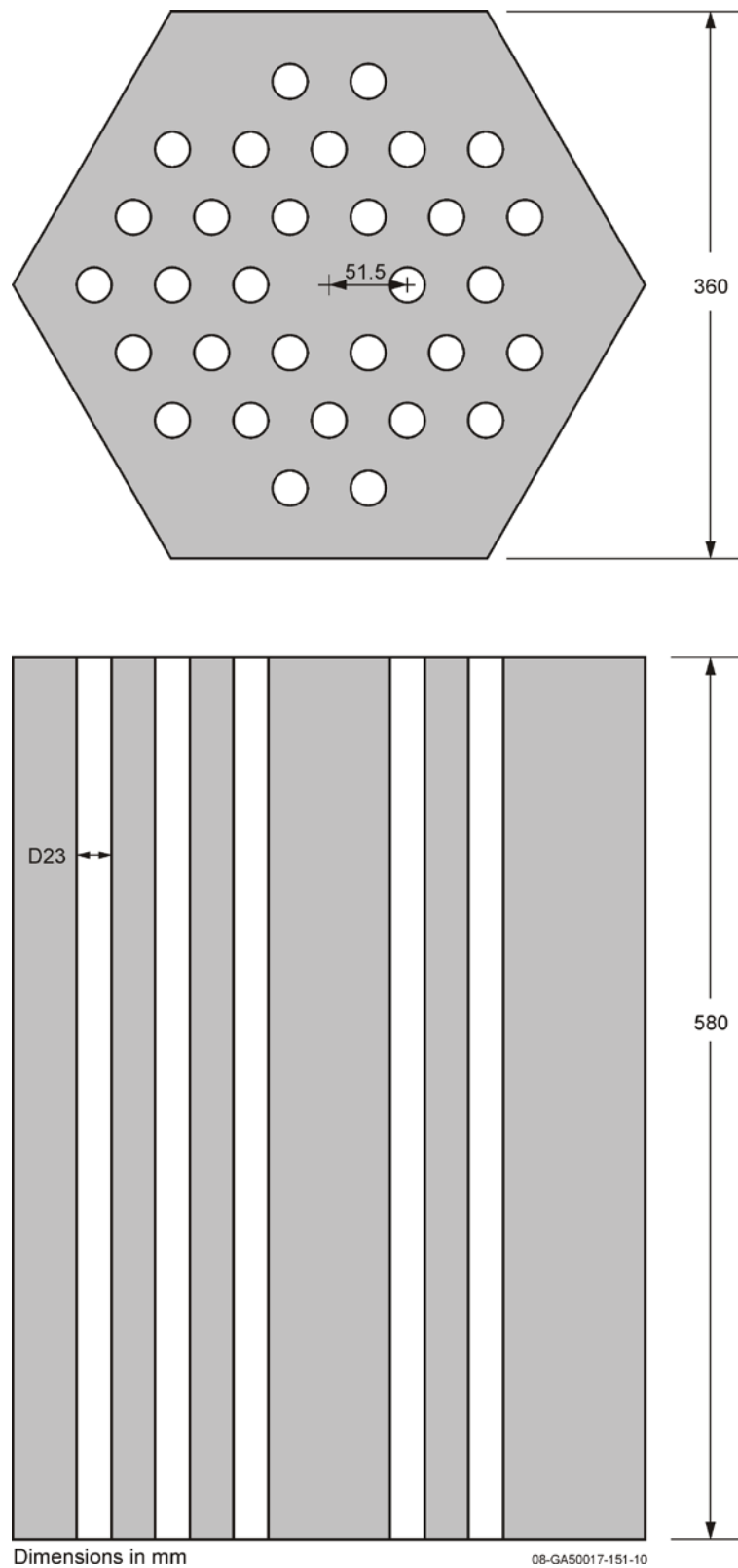
Figure 19. Replaceable reflector block for 31-pin fuel assembly. Dxx represents the diameter in xx (mm).

3.8 Helium Coolant

The primary coolant system is filled with helium at normal atmospheric pressure and was not in operation during fuel loading. Impurity concentrations during initial physics tests were negligible.

Helium gas enters the core after reversing at the upper plenum in the reactor vessel. The gas is heated as it flows downward through the fuel elements in each core region and leaves the reactor before passing through an inner tube of the outlet gas duct after mixing in the hot plenum.

3.9 Reactor Core Configuration

The HTTR reactor was assembled sequentially by replacing dummy blocks positioned in fuel locations with actual fuel blocks, thus obtaining various critical configurations. Two reactor-core configurations are analyzed in this study. Figure 20 depicts the 19-fuel column core, characterized by the annular fuel region. Figure 21 represents the fully loaded core with 30-fuel column. The CR position is measured from the bottom of the active core. Table 7 shows the CR positions for both critical configurations.
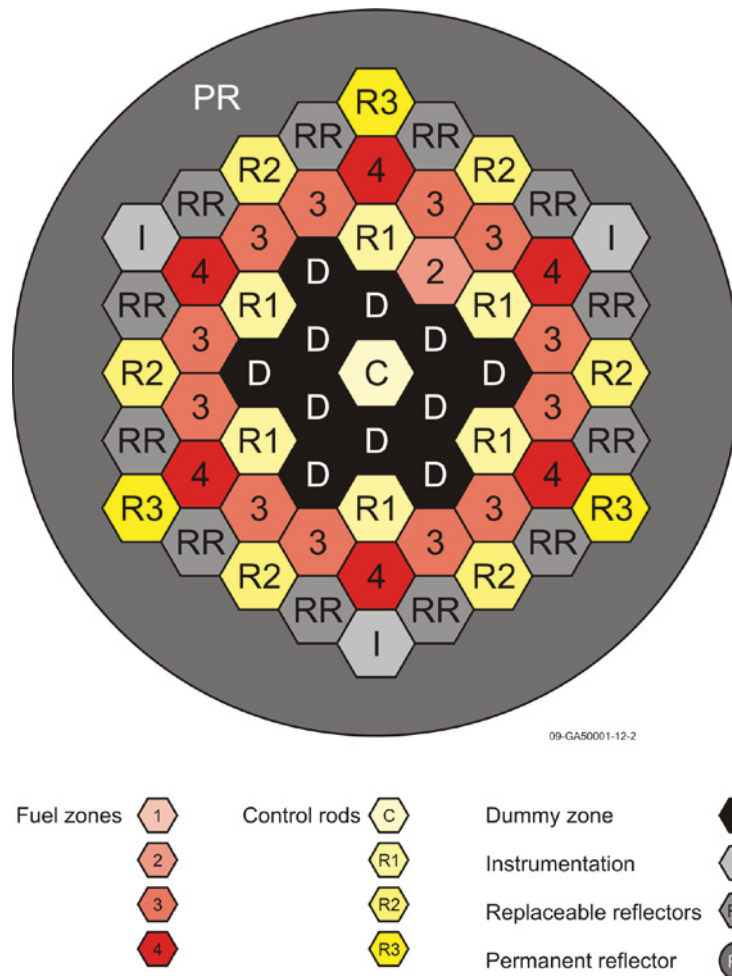
Figure 20. HTTR core positions (19-fuel columns).

08-GA50017-167-2
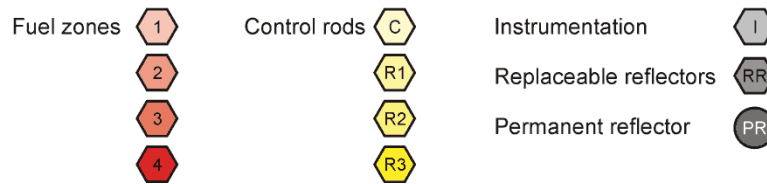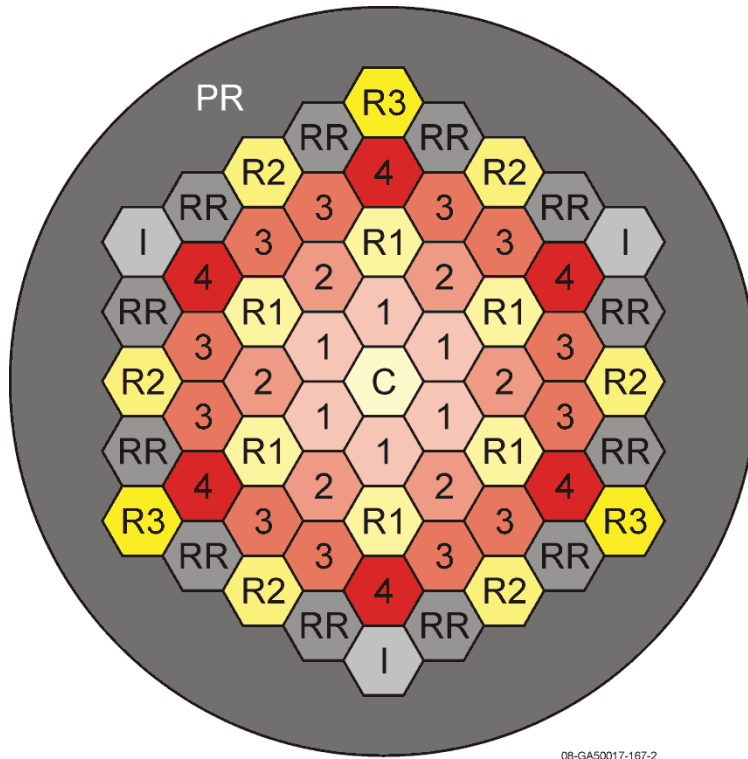
Figure 21. HTTR core positions (fully loaded, 30-fuel column core – no dummy fuel columns).

Table 7. Critical rod positions.

Number of Fuel Columns	Critical Rod Position [cm]/(axial level from top core)			
	C	R1	R2	R3
19	173.9/(4th)	405.0/(FW)*	332.5/(2nd)	405.0/(FW)*
30	177.5/(4th)	177.5/(4th)	177.5/(4th)	404.9/(FW)*

* FW – Fully Withdrawn

4. COMPUTER CODES

4.1 DRAGON 4

DRAGON 4 [10] solves the linearized version of the Boltzmann transport equation and includes cross-section generation capabilities. One of the great advantages of the DRAGON 4 code is in its simplicity for modeling, which allows the user to become proficient with the code in a short period of time. The variety of solution methodologies is another great asset of the code. The collision probability (CP), method of characteristics (MOC), and discrete ordinates (Sn) methods were used in during the performance of this work. In addition, the DRAGON code includes a 3-D capability by projection of the third dimension onto a 2-D plane with an MOC solution. The DRAGON 4 options used for the cross-section generation in this report include:

1. A transport correction based on the linearly anisotropic (P_1) within group scattering used to correct the library cross-sections

4. A self-shielding calculation based on the subgroup method

5. The Hebert double heterogeneity treatment in the fuel compacts

6. Use of the CP method with a P1 leakage model provides the flux solution in 281 groups

7. Spatial homogenization and the energy condensation into 26 groups.

The main limitation of the current version of the code is the geometric specification of a hexagonal block. The 2-D block geometry is built based on a smaller hexagonal unit cell leading to the presence of jagged edges at the block periphery. This introduces small errors with the boundary condition and additional moderator into the block calculation. In order to conserve the graphite mass in the model, the peripheral graphite density is adjusted.

The DRAGON 4 code has been successfully used in high temperature reactor (HTR) applications [15], and it is a well established nuclear analysis tool.

4.2 INSTANT

INSTANT is a neutron transport solver developed at INL and programmed in Fortran 90. Its discretization scheme is based on the second-order PN equation with the hybrid Finite Element Method [16,17]. This same variational nodal formulation for the spherical harmonic equations has been successfully used in the past with the VARIANT code, which is a well-established neutronics tool.
INSTANT includes a mesh manager to facilitate calculations on triangular, hexagonal, and Cartesian geometries in both 2D and 3D. Its parallelization includes domain decomposition with MPI to take advantage of the development on supercomputing techniques. Current plans are to integrate depletion, transient, and multiphysics frameworks to support design of different types of advanced reactors. Different transport solution schemes like the first-order SN with the discontinuous FEM, MOC, the second-order SN with the continuous FEM are planned to be implemented in the future.

4.3 MCNP

MCNP [18] is a general purpose Monte Carlo N-Particle (MCNP) code that can be used for neutron, photon, electron, or coupled neutron/photon/electron transport. The code treats an arbitrary three-dimensional (3-D) configuration of materials in geometric cells bounded by first- and second-degree surfaces and fourth-degree elliptical tori.

Pointwise cross-section data typically are used, although group-wise data also are available. For neutrons, all reactions given in a particular cross-section evaluation (such as ENDF/B-VI) are accounted for. Thermal neutrons are described by both the free gas and S (alpha, beta) models. For photons, the code accounts for incoherent and coherent scattering, the possibility of fluorescent emission after photoelectric absorption, absorption in pair production with local emission of annihilation radiation, and bremsstrahlung. A continuous-slowing-down model is used for electron transport that includes positrons, k x-rays, and bremsstrahlung, but does not include external or self-induced fields.

4.4 SERPENT

SERPENT is a 3-D continuous-energy MC reactor physics burnup calculation code, developed at VTT Technical Research Centre of Finland [19]. The code can analyze 2-D lattice physics calculations and more complicated 3-D geometries as well. The great advancement in the SERPENT code is the dual capability to generate homogenized multi-group constants for deterministic reactor simulator calculations and perform fuel-cycle studies involving detailed assembly level burnup calculations. Furthermore, the SERPENT code has two geometry models to describe fuel with double heterogeneities. The first is an implicit model that samples the positions of fuel particles inside the dispersed media during the transport simulation. The routine works by preserving the particle dimensions and packing fractions [20]. The second is an explicit model that reads the positions of fuel particles or pebbles from a separate input file. The particle/pebble distribution is covered by a 3D mesh used by the search algorithm in the geometry routine. These features make the SERPENT code very attractive for the current HTR benchmarking and analysis efforts.

4.4.1 MCNP-to-SERPENT geometry converter

For this project, a semi-automated program that takes MCNP geometry input and converts it to SERPENT geometry has been developed. This Python program performs the following tasks, allowing the over 1,000-line HTTR MCNP model [6] to be converted to a SERPENT input with only changing and adding about twenty lines:

- Converts surface types when there is a direct or trivial conversion, so 'so r' becomes 'sph 0 0 0 r'

- MCNP repeats are expanded so '2 3R' becomes '2 2 2 2'

- MCNP macro-bodies are converted by switching them to either an intersection of the equivalent surfaces if the inside of the macro-body is needed, or a union of the surfaces if the outside of the macro-body is needed

- Since SERPENT material definitions contain a density, but in MCNP the density is a property of the cell, conversion makes a dictionary of all the densities that cells use, and then generates a new material definition for each density and finds the proper material identification for use with each cell.

- Simple unions are converted into the equivalent set of intersections, so '(A : B)' becomes 'A B', '-A B', 'A –B,' and 'A B (C : D)' becomes 'A B C D', 'A B -C D' and 'A B C -D'

- Lattices are checked to see if an equivalent SERPENT lattice exists, and if so, it is converted

- When constructs that the script does not convert are identified, a %CONVERT comment is put in the output so that the user can find the unconverted portions

- The program will convert BUT LIKE cells by finding the original and making the needed modifications

- The program checks for features allowed in MCNP but not SERPENT, including lattices directly inside other lattices and having universes used in different levels of number of universes

- Rotations are partially handled by rotating the surfaces and some types of lattices

- The conversion code transforms the surfaces of subuniverses that rotated by being included in a universe that is rotated

- The hexagonal lattices are rearranged when they are rotated by 60 degree multiples

- Since the other steps sometimes generate multiple equivalent universes and surfaces, duplicates are searched and removed.

4.4.2   SERPENT testing

Several different inputs were created for testing the SERPENT code for very high temperature reactors (VHTRs). The simplest test was a cell level graphite fuel compact. This consists of TRISO particles inside a graphite fuel compact as shown in Figure 22. Both a SERPENT model and a MCNP model were created. There was about a 76-pcm difference between MCNP and SERPENT as shown in Figure 23. The flux tallies matched closely throughout the entire range of the spectrum.
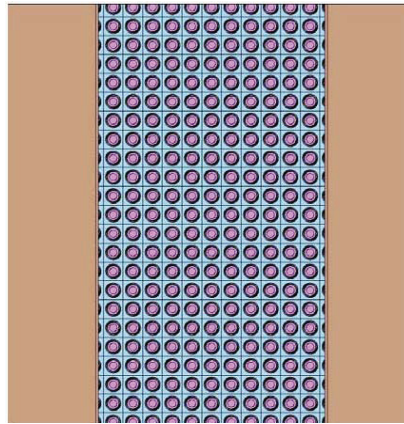
Figure 22. Fuel compact in SERPENT.
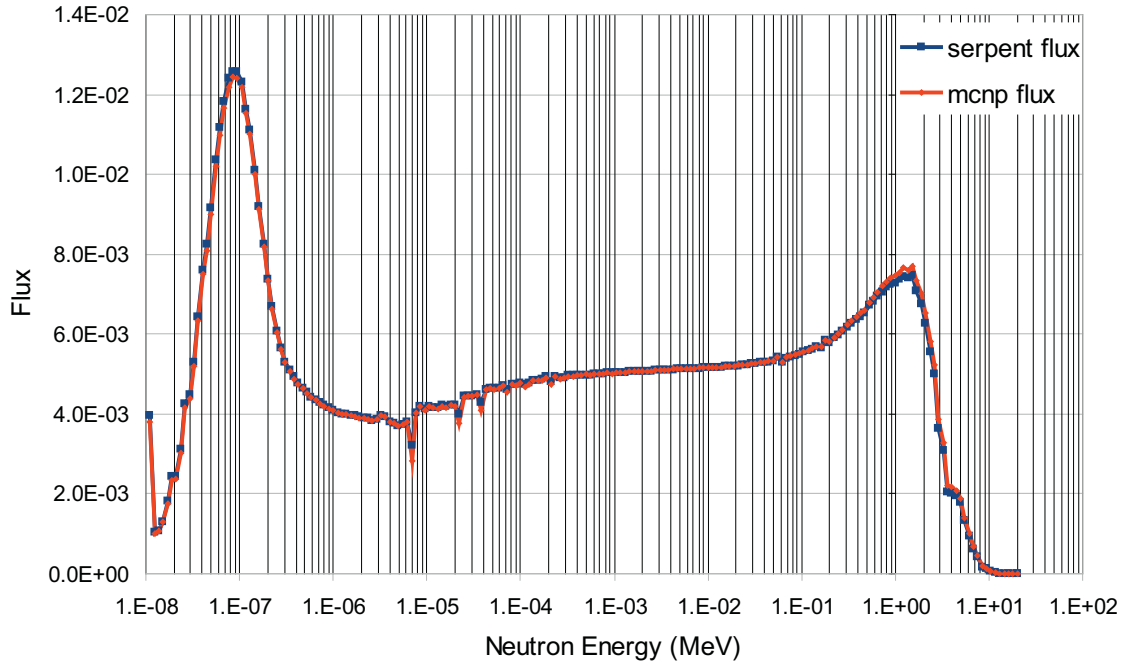
Figure 23. Flux comparison.

Two other inputs were created for SERPENT. The first was a block level input that was created to test the spectrum, and the second was a full HTTR input that was used to generate cross-section data. This is the first study to verify the cross-section generation capabilities of SERPENT in HTRs conducted at the INL. The output of SERPENT is in Octave formatted files. These need to be converted to a usable format, so two scripts were created. The first creates an ISOTXS file based on the SERPENT output, and the second creates a hexlib file from the SERPENT output.

4.5   HEXPEDITE

Nodal methods are characterized by reducing a multidimensional partial differential equation (PDE) i.e. neutron diffusion equation, into a set of coupled Ordinary Differential Equations (ODEs) by transverse integration of the PDE over a homogenized "node" or cell. Nodal methods have been shown to allow reasonably accurate solutions over a coarse mesh while retaining the simple coupling structure of finite difference methods. These two features make nodal methods attractive in that reasonably high accuracy can be achieved in a short time compared to other numerical methods.

In hexagonal-z or prismatic geometry, the 3-D flux solution over a prismatic node is split into four 1-D transverse averaged flux equations that are coupled by a leakage source term. These equations are formed by integrating over the nodal flux solution separately in each of the four directions perpendicular to the faces of a prismatic node. The transverse integrated flux is then scaled by the surface area of each face perpendicular to a given directionally dependent transverse integrated flux to get the equations in terms of averaged flux values. A Green's function solution is then applied to the resulting one-dimensional, transverse averaged ODE. The Green's function solution to transverse averaged diffusion equation (equivalently the Sturm-Liouville Operator) can be expressed in an integral form in terms of a source integral and boundary values of the net current on each node. The spatial coupling between two adjacent nodes is formed by requiring that the transverse averaged flux from one node be equal to the transverse averaged flux of an adjacent node. Additionally, the net currents at adjacent nodal interfaces

32

are also assumed equivalent, which is a physically accurate assumption. The result of these two spatial couplings is a tri-diagonal matrix system that can be solved for the net currents at the nodal interfaces.

Despite the analytical nature of the Green's function solution for the transverse averaged flux, the flux solution from the previous iteration must be expanded over a polynomial in order to generate a shape approximation for the fission/scattering source term. Additionally, the net current solutions adjacent to a node of interest are used to approximate a second order polynomial expansion for the leakage source term. The problem domain is split into coupled 1-D problems that can be solved in parallel, and the leakage and fission sources are solved iteratively.

Unlike in Cartesian geometry, the transverse integration procedure applied to hexagonal geometry introduces discontinuous terms in the sources, which are non-physical and purely mathematical in nature. The solution in HEXPEDITE is formed by first assuming that the discontinuous terms are negligible. The flux solution is then corrected by enforcing the node average neutron balance equation on the flux solution. For each directional sweep, the node balance is used to update the flux moments for the other sweeping directions across a given node.

5.   CROSS-SECTION GENERATION

5.1   Introduction

The European benchmark analysis group report [14] concluded that in order to better approach the experimental HTTR results, several effects had to be considered:

1. The detailed heterogeneity of the BPs and the fuel region in the whole-core calculation. INL has developed a new method to model the BP heterogeneity in the whole-core diffusion solver. This new technique is currently under testing within the HEXPEDITE code and has not been used in this report.

2. Using fine group structure in the whole-core diffusion calculation proposed by the German team or considering the neighbor effects in the transport calculation, proposed by the French team. Following the suggestion of the German team, the DRAGON 4 cross-section used in this analysis will be generated in 26 groups based on the FZJ structure [3]. New cross-section generation approaches that take into account neighbor effects were initiated and a summary included in Section 8.

3. Modeling axial effects of the BP heterogeneity. This effect was quantified in the European benchmark report [14] to be 1.5% Δk/k for the annular 19-column core and 2.2% Δk/k for the full core. For the DRAGON 4 models this effect was quantified with MCNP5 to be much larger in magnitude. The results show 2.38% and 2.94% Δk for the annular and fully loaded cores, respectively. Since no NGNP design has currently been selected, it is uncertain whether this will be an important issue in the future. The 3-D capabilities of the DRAGON 4 code are currently under testing to determine if these effects can be accurately modeled.

4. Treatment of the axial streaming in CR channels. This was quantified to be -1.8% Δk/k for the annular core and -1.3% Δk/k for the full core [14]. These effects can be modeled in the future with DRAGON 4, but might require some modifications to the source code in order to accurately describe the axial streaming effects in the large CR holes.

Since the current capabilities of the codes are limited, both the axial BP heterogeneity and axial streaming are corrected using the values provided in this section. Studies continue to improve the capabilities of INL codes when required for the NGNP.

The annular core cross-sections were all generated at 300 K. Cross-sections for the fully loaded core configuration were generated at 300, 340, 380, 420, 460, and 480 K.

5.2   Energy Group Structure

There are two energy structures in Table 8 used for the generation of cross-sections. These are based on the German studies included in the IAEA report [3]. DRAGON 4 calculations generated cross-sections with the 26-group structure, whereas the 4-group cross-sections were generated by SERPENT. A 4-energy-group structure was chosen due to the difficulties encountered in the generation of cross-sections with the initial 26 groups. SERPENT requires long run times to generate self-consistent cross-sections that can be used in deterministic benchmarking of HTRs. In locations far away from the fuel region where there is no significant source of fast neutrons, it is difficult to obtain statistically meaningful fluxes for the generation of consistent cross-sections. Apparently, no importance weighting is available in the code at this time in order to artificially direct neutrons into these tallies.

Table 8. Coarse group structure used in cross-section generation.

Group	4 group structure Upper Energy Boundary (eV)	Group	26 group structure Upper Energy Boundary (eV)
1	1.49E+07	1	1.492E+07
		2	7.408E+06
		3	3.679E+06
		4	6.721E+05
2	1.111E+05	5	1.111E+05
		6	1.931E+04
		7	3.355E+03
		8	1.585E+03
		9	7.485E+02
		10	2.754E+02
		11	1.301E+02
		12	6.144E+01
3	2.900E+01	13	2.900E+01
		14	1.370E+01
		15	8.320E+00
		16	5.040E+00
4	2.380E+00	17	2.380E+00
		18	1.290E+00
		19	6.500E-01
		20	3.500E-01
		21	2.000E-01
		22	1.200E-01
		23	8.000E-02
		24	5.000E-02
		25	2.000E-02
		26	1.000E-02

5.3   Modeling of Fuel Blocks

The DRAGON 4 energy and spatial flux calculations are performed with the full-block geometry in order to maximize the fidelity of the calculation. The model includes the annular compact with the double heterogeneity (DH) treatment in the fuel region, the gap between the compact and graphite sleeve, the graphite sleeve, and the cooling channel gap. The description of the microstructure comprises five layers including kernel, porous graphite, IPyC, SiC, and OPyC imbedded in the graphite matrix with the as-built specifications delineated in the benchmark document [4].

The fuel handling positions, dowels, and sockets were not included in the model. An example of the DRAGON 4 fuel-block model is shown in Figure 24. The size of the small hexagons is determined based on the fuel pitch. This approach introduces an error since the location of the BP rod is closer to the fuel than in the actual design (from a pitch of 5.45 cm to 5.15 cm). This effect was quantified in MCNP5 and shown to be insignificant—just a few pcm. In addition, the fuel-handling hole is not modeled explicitly; instead, the region is treated as a lower graphite density region. The geometry is closed with a white boundary condition at the periphery.

The main error introduced in the fuel model has to do with the jagged edges as seen in Figure 24. This geometric approximation changes the fuel-to-graphite ratio, which affects the neutron energy spectrum and, consequently, the microscopic cross-sections generated. This issue can be circumvented by decreasing the graphite density in the peripheral region in an effort to conserve the graphite content in the model. Unfortunately, this approach generates incorrect homogenized number densities in the DRAGON 4 code, because the graphite-to-block area is inconsistent with the design.
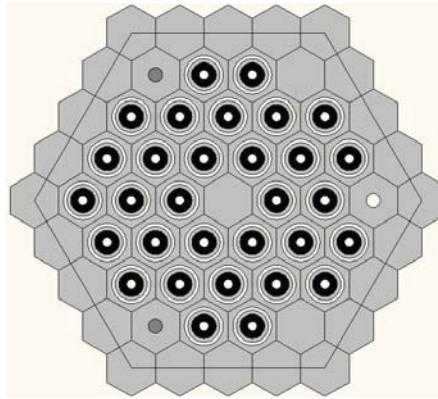
Figure 24. DRAGON 4 fuel-block model with 31 pins.

An MCNP5 (Figure 25) and a DRAGON 4 fuel-block model with 31 pins were developed for benchmarking purposes. A set of calculations was used to compare the two transport solutions. The DRAGON 4 models used in this study were spatially converged and solved via a CP solution with linear anisotropic current coupling.
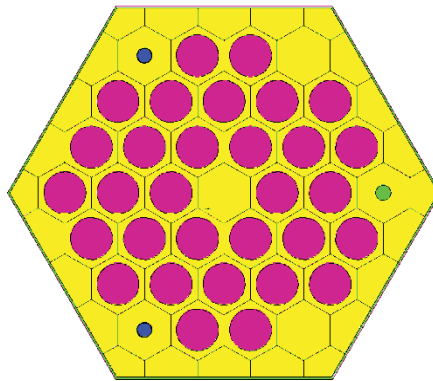
Figure 25. MCNP5 31-pin fuel-block model.

The first case, which contains homogeneous fuel without burnable poison (BP) pins, shows good agreement, while the presence of BP pins more than doubles the difference as shown in Table 9. Significant discrepancies in the solution appear with the double heterogeneity treatment. These differences are exacerbated in the presence of the BP pins. These calculations show that the DRAGON 4 model under-predicts MCNP5 by approximately 1% in the multiplication factor when modeling the full-block details. This 1% difference versus MCNP5 in the calculation of infinite fuel-block multiplication factor is expected to propagate into the whole-core calculation via the cross-sections. This does not mean that the DRAGON 4 results should be considered inadequate, since great uncertainty remains in the capability of all the codes to model this type of fuel accurately, and better benchmark data is not readily available.

Table 9. Benchmarking results DRAGON 4 versus MCNP5.

	Δk (pcm)
Homogeneous fuel no BP	84
Homogeneous Fuel with BP	190
DH treatment no BP	-518
DH treatment with BP	-1,034

Results from the DRAGON 4 calculations with both the reference design graphite density and the graphite density reduced at the periphery of the model are shown in Table 10. In addition, some of the APOLLO 2 and TOTMOS-DORT results [3] from the French and German programs are included for comparison. The 2-D APOLLO 2 model used a 172 group structure with homogenized fuel region cross-sections obtained from an initial 1-D cell calculation to treat the self-shielding. The German team used a TOTMOS 1-D cell calculation to generate homogenized fuel region cross-sections. A 2-D r-z DORT calculation was used to treat the BP axial heterogeneity. In contrast, The DRAGON 4 and APOLLO 2 models use an axial BP homogenized representation. Both DRAGON 4 models yield higher values of k_{inf} when compared to APOLLO 2. These differences can be attributed to a variety of reasons: fuel representation, leakage model, and fine group data, among others. The DORT results lie in between the two DRAGON 4 calculations.

Table 10. DRAGON 4 and APOLLO 2 results for the HTTR fuel blocks.

Fuel Block	Enrichment [$^w/_o$]	DRAGON 4 K_{inf}	DRAGON 4 K_{inf} ρ adjusted	APOLLO2 K_{inf}	2-D DORT K_{inf}
f343320	3.4	1.15789	1.11406	1.1065	1.1598
f393320	3.9	1.21318	1.16999	1.14991	1.2068
f433120	4.3	1.24450	1.20505	1.18391	1.2415
f433325	4.3	1.22372	1.17739	1.15656	1.2181
f483120	4.8	1.27936	1.23850	1.21366	1.2728
f523325	5.2	1.28021	1.23141	1.2038	1.2677
f593125	5.9	1.31702	1.27250	1.24481	1.3083
f633125	6.3	1.33291	1.28772	1.25798	1.3217
f633325	6.3	1.33334	1.28266	1.24962	1.3143
f673320	6.7	1.37305	1.32263	1.28423	1.3464
f723125	7.2	1.36883	1.32238	1.28937	1.3529
f793125	7.9	1.39189	1.34412	1.30862	1.3782
f793320	7.9	1.41127	1.35907	1.31733	1.3712
f943120	9.4	1.43421	1.38568	1.36335	1.4216

Fuel Block	Enrichment [$^w/_o$]	DRAGON 4 K_{inf}	DRAGON 4 K_{inf} ρ adjusted	APOLLO2 K_{inf}	2-D DORT K_{inf}
f993120	9.9	1.44483	1.39570	1.37213	1.4297

These differences in the DRAGON 4 modeling approach at the block level had to be further investigated to determine the effect on the cross-sections generated. The difference between the DRAGON 4 generic (reference design density) and corrected (modified peripheral graphite density) models were quantified, and the results are included in Figure 26 and Table 11.

The graphite-adjusted model yields a harder neutron spectrum due to the reduction of the moderator content in the infinite lattice calculation. The generic model produces a softer neutron spectrum that leads to neutron production cross-sections with a 3–8% error in the thermal range. Based on these results, it was decided to compute the macroscopic properties externally in order to obtain both the spectral effect from the graphite-density-adjusted calculation and retain number densities that are more consistent with the design. These macroscopic diffusion parameters were computed from the DRAGON 4 microscopic properties and the separately calculated homogenized number densities.

The geometric constraints in DRAGON 4 are impractical but still can be eluded. The DRAGON team has been working on the development of a flat-side hexagon configuration that will remove this limitation in the code. In addition, the new DRAGON 4 version will allow the precise positioning of various geometric features within the block, i.e. control rods.
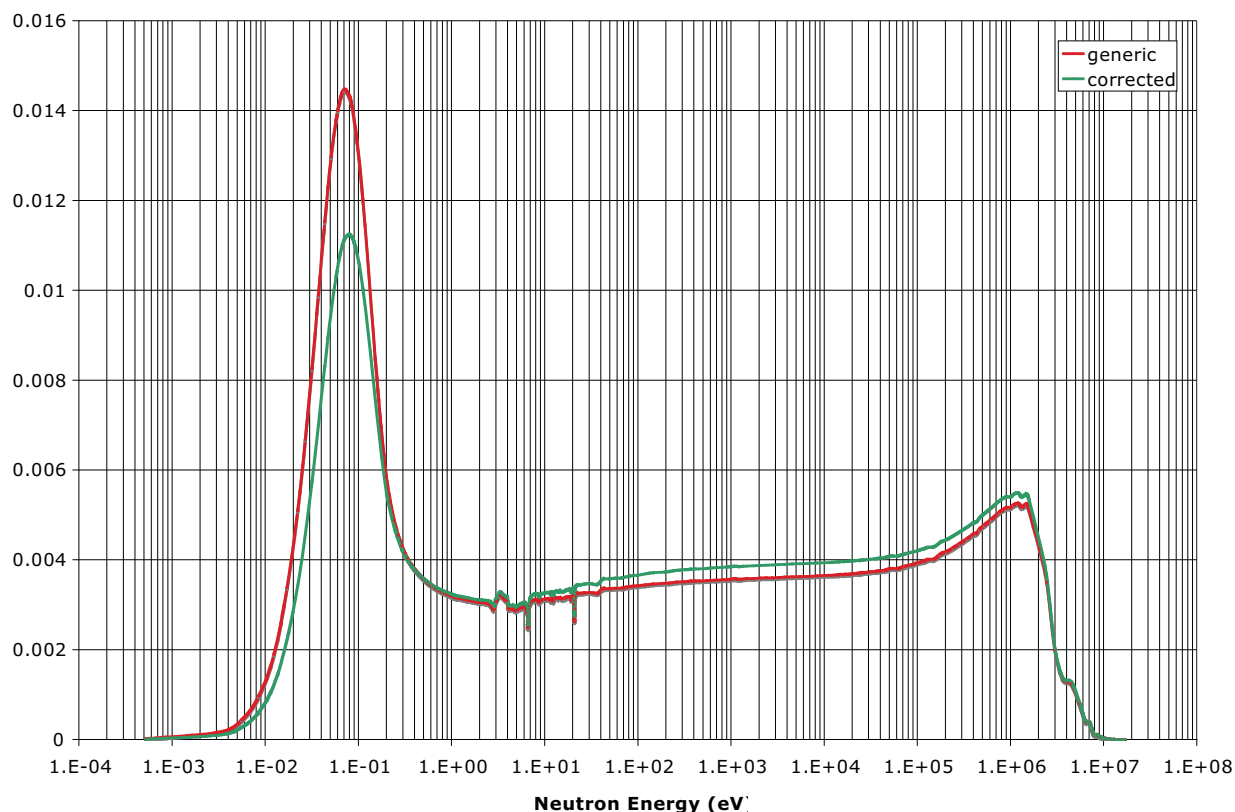
Figure 26. Change in the neutron-energy spectrum with and without adjustment of the peripheral graphite.

Table 11. Percent differences in $\nu\sigma_f$ with and without adjustment of the peripheral graphite.

Group	Generic Peripheral ρ	Adjusted Peripheral ρ	% Difference
1	1.18E-03	1.07E-03	-10.6
2	5.94E-04	5.38E-04	-10.5
3	2.01E-04	1.83E-04	-9.8
4	3.89E-05	3.72E-05	-4.6
5	5.18E-05	5.07E-05	-2.1
6	9.01E-05	8.94E-05	-0.8
7	1.55E-04	1.55E-04	-0.4
8	2.30E-04	2.30E-04	-0.2
9	3.85E-04	3.85E-04	0.0
10	5.31E-04	5.32E-04	0.2
11	7.18E-04	7.21E-04	0.4
12	1.10E-03	1.11E-03	0.7
13	1.11E-03	1.12E-03	1.0
14	1.80E-03	1.82E-03	1.1
15	4.59E-04	4.67E-04	1.5
16	4.41E-04	4.49E-04	1.7
17	4.24E-04	4.30E-04	1.4
18	1.65E-03	1.68E-03	1.3
19	2.65E-03	2.68E-03	1.2
20	4.51E-03	4.59E-03	1.7
21	4.83E-03	4.94E-03	2.1
22	6.25E-03	6.42E-03	2.7
23	8.14E-03	8.44E-03	3.5
24	1.16E-02	1.22E-02	4.4
25	1.84E-02	1.96E-02	6.0
26	2.66E-02	2.90E-02	8.2

5.4 Modeling of the Permanent Reflector

During the generation of the cross-sections for nonmultiplying media (i.e., regions with no fissile or fissionable material) participants of the CRP-5 benchmark used various techniques. The French approach used a 1-D cylindrical core solution to generate permanent reflector cross-sections with a single, representative fuel spectrum in a source-driven[14]. This study expands this technique for the analysis of the annular core in order to better account for the strong coupling between the various core regions. An R-Z solution of the annular core problem with homogenized regions is used for two purposes: (1) generate permanent reflector cross-sections, and (2) obtain neutron spectra in various core regions. These spectra are subsequently used as a surface source in a source-driven problem in order to better approximate the neutron spectrum and the cross-sections in the regions outside the active core.

The schematic of the R-Z cylindrical annular core used in the generation of relevant spectra for the various regions and the cross-sections for the reflector region is depicted in Figure 27. The model only

includes 18 fuel columns in order to avoid the azimuthal homogenization of the 19th fuel column. Therefore, the results should yield lower eigenvalues than a model with all of the fuel columns, but the spectra should still be well represented. The absorber regions are modeled as a ring with the equivalent surface area and volume as the design rods. The fuel region cross-section used in the annular R-Z model was generated from a 2-D fuel block model with the average fuel isotopic concentrations pertinent to that axial level. The fuel block was homogenized, but the energy structure was not collapsed in order to carry forward as much spectral information as possible. The model used a void boundary condition at the top and bottom regions and reflected at the center.

		9.13	10.5	18	19	54	55	90	90.5	126	127	127.5	162.0	178.5	195	212.5
		9.13	1.37	7.5	0.5	35.5	0.5	35.5	0.5	35.5	1.0	0.5	34.5	16.5	16.5	17.5
58	58	CRU	ABS1	CRU	1	DB	4	CRUDB	8	RR	ABS2	15	CRU	PR	PR	PR
116	58	CRU	ABS1	CRU	1	DB	4	CRUDB	8	RR	ABS2	15	CRU	PR	PR	PR
174	58	CRU	ABS1	CRU	1	DB	4	CRUDB	9	F1	GAS	15	CRU	PR	PR	PR
232	58	CRU	ABS1	CRU	2	DB	5	CRUDB	10	F2	GAS	16	CRU	PR	PR	PR
290	58	CRU	GAS	CRU	2	DB	5	CRUDB	11	F3	GAS	16	CRU	PR	PR	PR
348	58	CRU	GAS	CRU	2	DB	5	CRUDB	12	F45	GAS	16	CRU	PR	PR	PR
406	58	CRU	GAS	CRU	3	DB	5	CRUDB	13	F45	CRU	16	CRU	PR	PR	PR
464	58	CRU8	GAS	CR8	3	DB	6	CRUDB8	14	RR	CRU8	17	CRU8	PR	PR	PR
522	58	CR9	CR9	CR9	3	DB	7	CRUDB9	14	RR	CR9	18	CR9	PR	PR	PR

Where the following regions are defined.

CRU	Control Rod Guide Block - unroded
CRU8	Control Rod Guide Block 8th level - unroded
CR8	Control Rod Guide Block 8th level
CR9	Control Rod Guide Block 9th level
DB	Dummy Block
CRUDB	Mixed CRU and Dummy Block
CRUDB8	Mixed CRU8 and Dummy Block
CRUDB9	Mixed CRU9 and Dummy Block
ABS1/2	Neutron Absorber Region
GAS	Empty CR Position
RR	Replaceable Reflector Block
FX	Fuel Level X Block
PR	Permanent Reflector Block
X	Spectrum Tally Position

Figure 27. R-Z model of HTTR.

An Sn solution of the R-Z annular core model was obtained with DRAGON 4 using a 281-group structure and 14 discrete angles. A linear anisotropic representation was used for the scattering source. The results in Figure 28 show that the solution for the unrodded case converges at $k_{eff} = 1.005$, whereas the rodded configuration converges at $k_{eff} = 0.97$. This is a good result if one takes into account the fact that this model is missing 1 fuel column, which would generate a near-critical reactor.

Since no leakage model was used in the R-Z transport calculation, the diffusion coefficients for the permanent reflector region were calculated from the available data using *Equation (1)*. The average scattering angle cosines used in the calculation were determined from a permanent reflector block calculation with reflective boundary conditions.

$$D = \frac{1}{3\left(\Sigma_T - \overline{\mu}_0 \Sigma_s\right)}$$

(1)
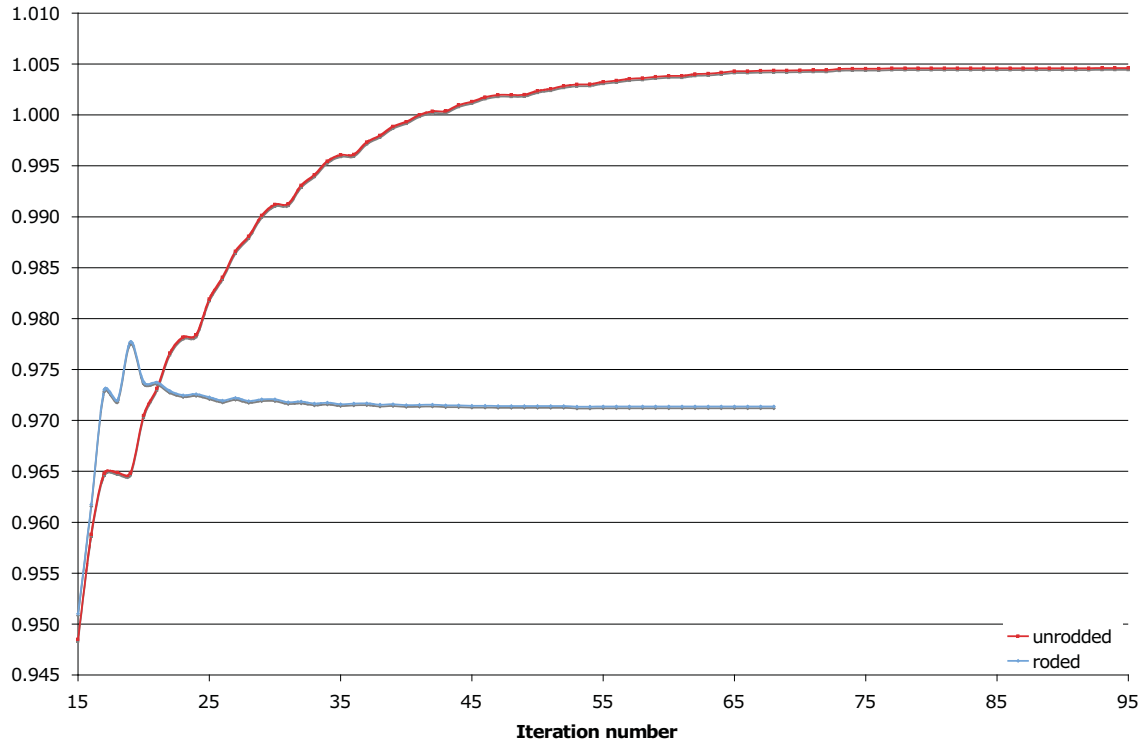
Figure 28. Solutions to the R-Z core problem.

The spectra obtained from the full-core unrodded model are used in the generation of cross-sections for the dummy, replaceable reflector, and CR detailed 2-D models. Figure 29 shows some of the spectra from various regions in the core for the unrodded solution. The regions near the active core (9 and 15) are characterized by a low thermal peak and a high fast peak, whereas regions with considerable moderation (6 and 7) include a high thermal peak and a relatively flat epithermal and fast regions.

Two sets of permanent reflector cross-sections for the 30-column core are produced in this study. The first set (referred as PR-I) is based on the 19-fuel column 2-D calculation with the annular core configuration at the various temperatures of interest. This model assumes that the neutron energy spectrum obtained at the reactor periphery is insensitive to the fuel located in the inner rings of the core. A second set of cross-sections (referred as PR-II) is developed using a single block configuration with a source on two consecutive sides of the block, and a representative fuel spectrum of the average core enrichment. This last geometry was closed with a reflective boundary condition.
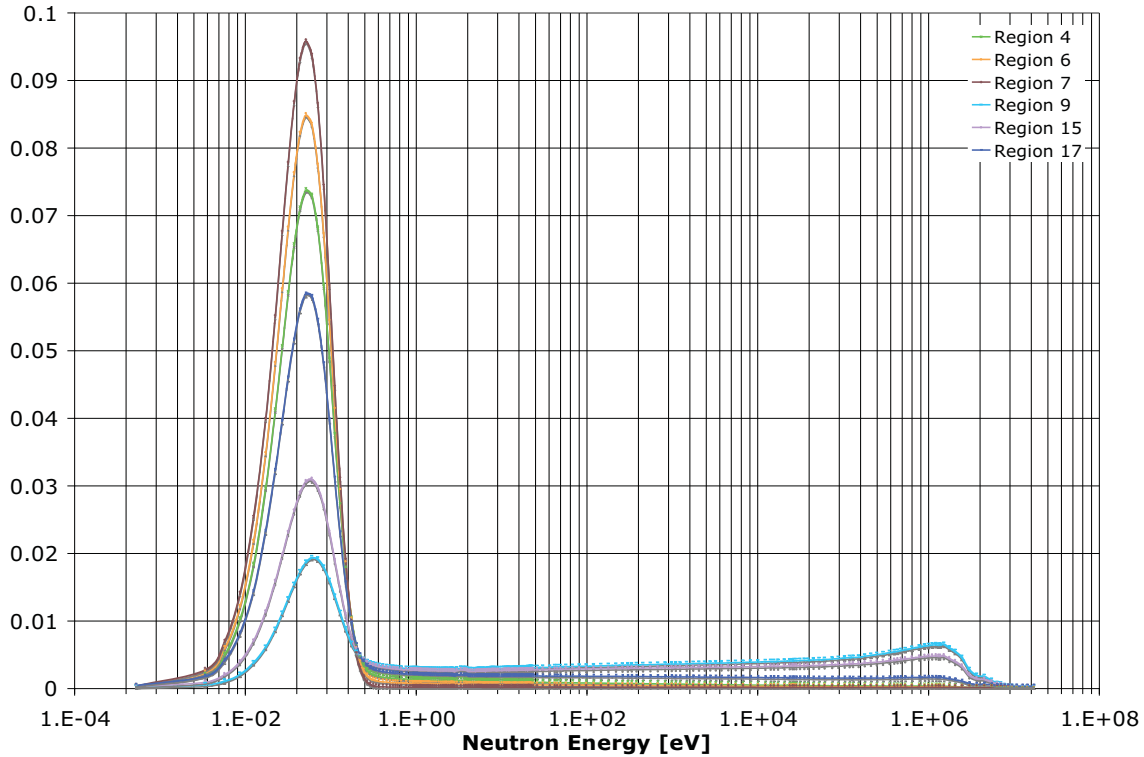
Figure 29. Neutron energy spectra in various locations of the annular core.

5.5 Modeling of the Replaceable Reflector, Dummy, and Control Blocks

The generation of the cross-sections for the replaceable reflectors, dummy, and control blocks employs two consecutive calculations in DRAGON 4. The first calculation places an isotropic surface source, based on the spectrum calculated from the R-Z model for that specific core location, at the periphery of the block. A void boundary condition is specified and the flux solution is obtained by solving a source-driven problem. This first computation generates the bulk of the cross-sections used in the HEXPEDITE runs. The second calculation is intended only for the generation of the diffusion coefficients. This computation uses a surface source specified with a trace amount of fissile material with a modified neutron spectrum that is consistent with the first calculation. This second model is closed with a reflected boundary condition, and the flux solution is obtained via a k-eigenvalue problem with a P_1 leakage model.

The standard control rod design used in the models is depicted in Figure 15 of this report. The JAERI memorandum [4] contains the specific differences in each CR design, which include variations in the number, diameter, and length of the CR holes, as well as the block height. Due to geometric limitations of DRAGON 4, the large CRs insertion holes of 6.15 cm were limited to 5.6 cm, effectively eliminating the gap between the CR and the CR hole. The graphite mass was conserved by reducing the block graphite density. Table 12 shows the correction used to reduce the graphite density in the fuel-handling hole (FHH) region and the correction of the block graphite density to maintain a consistent mass with the design block. The table includes the block across-the-flats (AF) distance, height, number of CR holes and the radius. The parameters used to build the DRAGON 4 model include the side length of the hexagon (Hex L), the across-the-flats distance of the hexagon (Hex AF). The DRAGON 4 representative block AF distance is also included.

Table 12. Calculation of graphite density corrections in the CR models.

HTTR DESIGN					
JAERI Report Figure	Fig. 10	Fig. 11	Fig. 12	Fig. 13	Fig. 14
AF (cm)	36	36	36	36	36
Height block (cm)	58	58	58	58	48
# CR holes	3	3	3	2	0
CR hole radius (cm)	6.15	varies	varies	7	0
DRAGON MODEL					
Based on INL Figure	Figure 15	Figure 15	Figure 15	Figure 15	Figure 17
Hex L (cm)	6.5	6.5	6.5	6.5	3
Hex AF (cm)	11.26	11.26	11.26	11.26	5.20
Approx. Block AF (cm)	39	39	39	39	36
# CR	3	3	3	2	0
CR hole radius (cm)	5.6	5.6	5.6	5.6	0
# Hex	19	19	19	19	61
Corrections					
FHH graphite ratio	0.6564	0.6564	0.6564	0.6564	0.5849
Block graphite ratio	0.7906	0.7432	0.7360	0.7972	0.9987

Similar corrections are used in the replaceable reflector and dummy fuel block models. Several axial heterogeneities (shorter insertion holes) are also corrected to maintaining consistency with the actual design. These are included in Table 13 and Table 14 for the replaceable reflector (RR) and dummy blocks (DBs), respectively.

Table 13. Calculation of graphite density corrections in the RR models.

HTTR DESIGN					
JAERI Report Figure	Fig. 15	Fig. 16	Fig. 17	Fig. 18	Fig. 19
AF (cm)	36	36	36	36	36
Height block (cm)	58	58	48	58	48
# cool. holes	33	31	6	0	0
Cool. hole radius (cm)	1.15	1.15	2.7	0	0
DRAGON MODEL					
Based on INL Figure	Figure 18	Figure 19	N/A	Figure 17	Figure 17
Hex L (cm)	2.97	2.97	3.15	3.00	3.00
Hex AF (cm)	5.15	5.15	5.46	5.20	5.20
Approx. Block AF (cm)	35.68	35.68	37.80	36.00	36.00
# cool. holes	33.00	31.00	6.00	0.00	0.00
Cool. hole radius (cm)	1.15	1.15	2.70	0.00	0.00
# Hex	61.00	61.00	61.00	61.00	61.00
Corrections					
FHH graphite ratio	0.6564	0.6564	0.6353	0.6982	0.6353
Block graphite ratio	0.9716	0.9735	0.9574	0.9991	0.9989

Table 14. Calculation of graphite density corrections in the DB models.

HTTR DESIGN			
JAERI Report Figure	Fig. 20	Fig. 21	Fig. 22
AF (cm)	36	36	36
Height block (cm)	58	58	58
# CR holes	3	3	3
CR hole radius (cm)	6.15	2.05	3
DRAGON MODEL			
Based on INL Figure	Figure 15	Figure 15	Figure 15
Hex L (cm)	6.5	3	3.47
Hex AF (cm)	11.26	5.2	6.0
Approx. Block AF (cm)	39	36	31.23
# CR	3	3	3
CR hole radius (cm)	5.6	2.05	3
# Hex	19	61	37
Corrections			
FHH graphite ratio	0.6564	0.6564	0.6564
Block graphite ratio	0.8550	0.9911	0.9973

6.   CORE SIMULATION

Full-core calculations are performed with the HEXPEDITE nodal diffusion solver, based on the Nodal Green's Function Method (NGFM), the INSTANT transport code, and the SERPENT MC transport code. The MC model can explicitly represent the geometric detail of the core structures, whereas HEXPEDITE and INSTANT solve homogenized regions that represent the actual blocks in the core.

6.1   HEXPEDITE Model

The HEXPEDITE code provides the whole-core flux solution for a given set of diffusion theory-based cross-sections. There are a total of 61 hex-planar nodes in the core and two radial layers of permanent reflector blocks. Details of the 19 and 30 column core designs are included in Appendices A and B, respectively.

The permanent reflector thickness had to be approximated since HEXPEDITE and INSTANT can only model full blocks. Table 15 shows the HTTR design specifications for the permanent reflector thickness at the various locations in the core and the equivalent block thickness. The average permanent reflector thickness is approximately 2.214 blocks. The DRAGON-HEXPEDITE models used in this report have two permanent reflector blocks in all locations. The effect was quantified with models containing two and three permanent reflector blocks. The two-block model resulted in an eigenvalue of 1.0273, while the result for the three-block model was 1.0331. These values confirm that the permanent reflector design is not asymptotic in nature, since leakage has a significant effect on the core eigenvalue. The final results need to be modified to include this effect. For the average thickness of 2.214 blocks, the correction is approximated to be near 0.1% Δk.

Table 15. Permanent reflector thickness.

Hex-row	Ref Thickness (cm)	Thickness in 36-cm blocks
1	49.6	1.55
2	65.37	2.04
3	76.34	2.39
4	81.95	2.56
5	81.05	2.53

There are nine axial regions in the HEXPEDITE 3-D core model. These were divided in two cells during an axial convergence study for a total of 18 axial nodes. In the annular core configuration, two HEXPEDITE models have been developed: one based on SERPENT cross-sections and the second one based on DRAGON 4 cross-sections.

The isothermal temperature coefficients (ITCs) were determined from full-core multiplication factor calculations with the following equation:

$$\rho = \frac{k_{T_1} - k_{T_2}}{k_{T_1} k_{T_2}} \frac{1}{(T_1 - T_2)} \tag{2}$$

During the ITC measurement in the HTTR, the CRs were adjusted to maintain criticality. The CR positions achieved during the ITC measurement are not currently available to the authors. For the multiplication factor calculations, the CRs are kept in the critical configuration delineated in Table 7. Therefore, the calculated ITCs are not completely representative of the core configuration during the measurement.

6.2   INSTANT Model

The INSTANT model was exactly based on that of HEXPEDITE in order to generate the reference solution. Figure 30 shows the layout of the full core model with the various material regions. The calculation uses a P_1 solution method over 2286 cells.
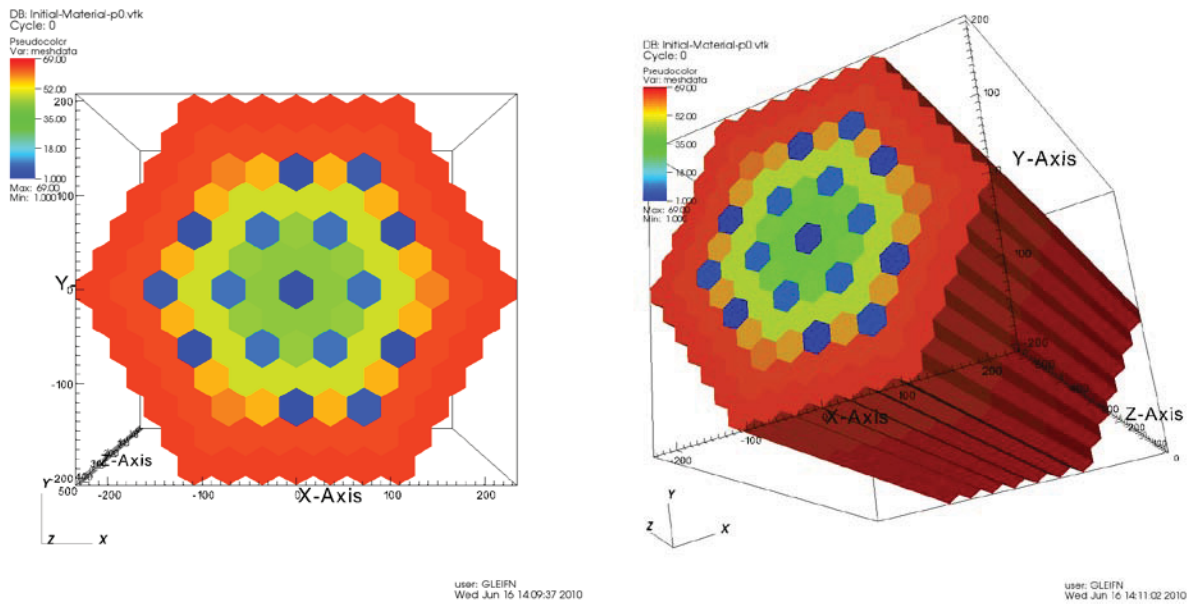
Figure 30. Layout of the INSTANT full core model.

6.3   SERPENT Model

The SERPENT model used in this study is based on the MCNP5 model from the IRPHEP work [5,6]. The hex-plane view of the HTTR model in SERPENT shown in Figure 31 includes a cylindrical permanent reflector, the 31 and 33 pin fuel blocks forming the annular core, the CR block, and in a darker shade, the DBs. It depicts the critical configuration with the central CRs inserted. Figure 32 provides the axial view of the critical configuration in the model with the CR insertions from Table 7. The detail of the TRISO dispersion in the fuel is displayed in Figure 33.
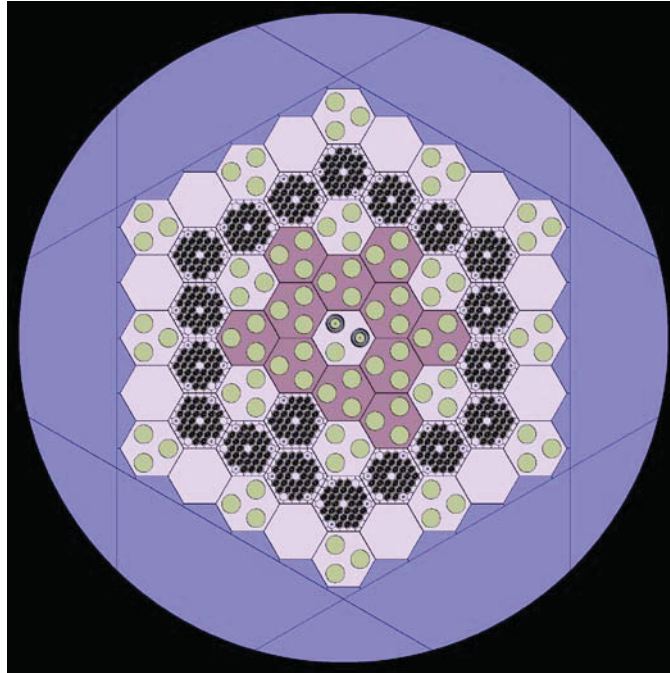
Figure 31. Hex-plane view of the HTTR SERPENT model.
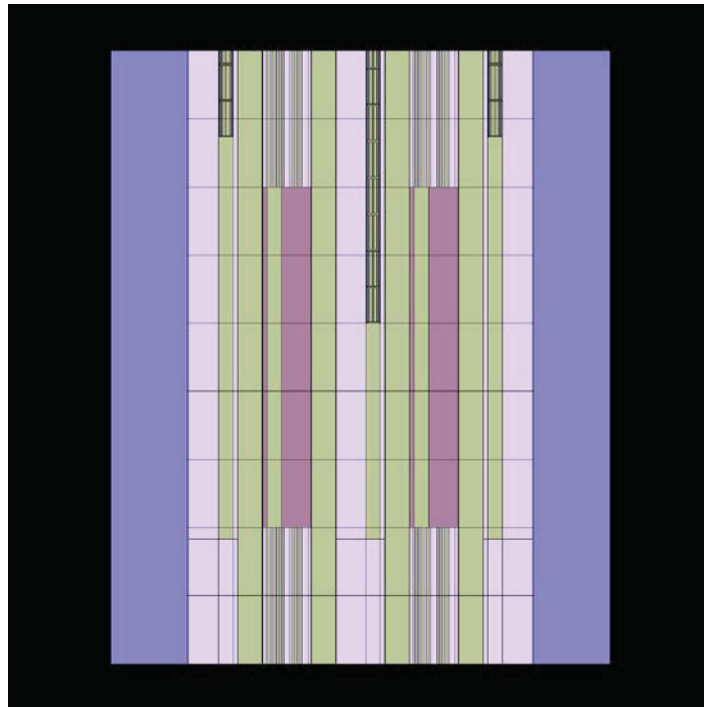
Figure 32. Axial-plane view of the HTTR SERPENT model.
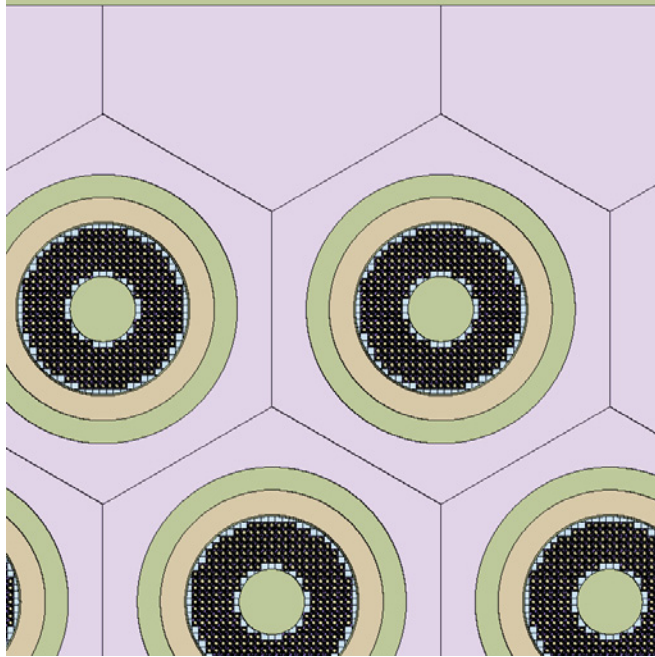
Figure 33. TRISO detail within the fuel compact in the HTTR SERPENT model.

7.   RESULTS

This section of the report includes two subsections. The first subsection discusses the results from the MC code SERPENT and the verification of the HEXPEDITE nodal diffusion code. The second section is primarily focused on the calculation of the critical configuration with DRAGON 4-HEXPEDITE for both annular and fully loaded cores.

7.1   Verification of the HEXPEDITE Code

The first test conducted to verify the HEXPEDITE multiplication factor calculation was a model of an infinite lattice block calculation with cross-sections from DRAGON 4. The results obtained for this simplified geometry are in excellent agreement. The difference between the DRAGON 4 and HEXPEDITE results is 37 pcm.

The verification of the core multiplication factor calculation with more heterogeneities than that of the single block is obtained from the INSTANT reference solution. Table 16 includes the results from the INSTANT and HEXPEDITE calculations with the same DRAGON-4 generated cross-sections. The results show excellent agreement with a difference of 50 pcm.

Table 16. Eigenvalue calculation results with DRAGON 4 data.

DRAGON 4 HEXPEDITE	DRAGON 4 INSTANT
1.02459	1.02409

A second verification method was attempted using cross-sections from the SERPENT code. The results from these calculations are shown in Table 17. The 26 group data generated with SERPENT showed significant differences in the values of the diffusion coefficient when compared to DRAGON 4 data. The calculated eigenvalue with this SERPENT data is almost 4000 pcm lower than the reference MC calculation. The values change significantly when DRAGON 4 diffusion coefficients are used instead, increasing the eigenvalue 1793 pcm above the reference solution. The four group structure generated with SERPENT also produced a significant low value that deviates roughly by 3000 pcm. These large differences imply that the cross-section generation capabilities with SERPENT need to be further developed.

Table 17. Eigenvalue calculation results with SERPENT data.

SERPENT MC	SERPENT HEXPEDITE I (26 grp)	SERPENT HEXPEDITE II[a] (26 gr)	SERPENT HEXPEDITE (4 gr)
1.0370 ± 0.00003	0.99729	1.05493	1.00708
(a) with diffusion coefficients from DRAGON 4			

7.2   Full Reactor Calculation Results

The results from both critical configurations are included in Table 18. Two HEXPEDITE results are included for the fully loaded core (30 columns) with the two permanent reflector calculation methods (PR-I and PR-II). The first method is based on the R-Z annular core calculation and the second on the single block with a surface source. MCNP5 and SERPENT results are also included for comparison.

Table 18. Multiplication factor results for the annular and fully loaded critical core configurations.

Number of Fuel Columns	Experiment $k^{(a)}$	DRAGON 4 HEXPEDITE	DRAGON 4 HEXPEDITE$^{(b)}$	MCNP5$^{(c)}$	SERPENT
19	$1.0048 \pm (>?)$	1.0212	1.0262	1.0276 ± 0.0001	1.0370 ± 0.00003
30 (PR-I)	$1.0025 \pm (>3.6\%)$	1.0230	1.0394	1.0229 ± 0.0001	N/A
30 (PR-II)	$1.0025 \pm (>3.6\%)$	1.0179	1.0343	N/A	N/A
(a) Corrected for instrumentation bias [5,6].					
(b) Corrected for axial streaming and BP homogenization effects.					
(c) From the IRPHEP reports [5,6].					

All results show a 2–3% bias that is consistent with the MC results. It is noteworthy to mention that similar runs with other MC codes also show significant deviations in the core multiplication factor. This 2–3% bias is believed to originate with the large uncertainty in the graphite impurity level, and to a lesser extent, with the continuous energy data libraries for graphite and U_{235} [5,6,21]. In addition, the resonance scattering models included in the MCNP codes, and potentially SERPENT, are in question [22].

In the annular 19-fuel column core there is very good agreement between HEXPEDITE and MCNP5, but it is coincidental in nature. The MCNP5 models use the same evaluated data files, but geometrically, they are not identical and the material properties are not exactly the same. This discrepancy stems from the fact that the reference design document [4] was not available to INL when the MCNP5 models were built [5,6].

The HEXPEDITE model contains the as-built atomic densities and a better geometric description of the DB design used in the 19-column core critical. This effect was approximately quantified with a DRAGON-HEXPEDITE calculation to be 0.3% Δk, which together with 0.1% Δk correction for the permanent reflector approximation would increase the multiplication factor to 1.0302. This result is still in good agreement with the MCNP5 model and is more representative of what is expected in diffusion to transport comparisons. The SERPENT model, which is based on the MCNP5 model, also uses continuous energy ENDF/B-VII data and yields roughly 900-pcm higher eigenvalues than MCNP5.

The corrected full-core loading results show a significant departure from MCNP5. This core configuration does not contain dummy fuel blocks, which removes that uncertainty from the calculation. Unfortunately, the axial BP correction becomes quite large (3% Δk). The two HEXPEDITE results (I and II) also show a significant sensitivity to the approach used in the generation of permanent reflector cross-sections (500 pcm). Only the second approach falls within the uncertainty of the experiment.

The multiplication factors at several isothermal fully loaded core temperatures are listed in Table 19. In addition, some results from the CRP-5 benchmark [3] are also included for comparison. The DRAGON-HEXPEDITE results (PR-I) with the R-Z annular solution for the permanent reflector cross-sections are significantly higher than the rest. The other set of DRAGON-HEXPEDITE (PR-II) results are similar to those generated with DELIGHT-CITATION, but are still significantly higher than the other codes.

Table 19. Eigenvalue calculation results for the fully loaded core at various temperatures.

Temp. [K]	WIMS-D/4 JAR	DELIGHT CITATION	APOLLO2 CRONOS2	DRAGON 4 HEXPEDITE PR-I	DRAGON 4 HEXPEDITE PR-II
300	1.0023	1.01696	1.00395	1.02303	1.01789
340	0.9930	1.01199	0.99724	1.01588	1.01061
380	0.9844	1.00653	0.99088	1.00878	1.00321
420	0.9768	1.00110	0.98455	1.00172	0.99592
460	0.9699	0.99570	0.97823	0.99486	0.98890
480	0.9665	0.99015	0.97525	0.99149	0.98544

The isothermal temperature coefficients calculated with the data from Table 19 using *Equation (2)* are included in Table 20. The HEXPEDITE results are over 40% higher than the experimental results, but these were measured at different CR positions, which in this reactor have significant effects on the entire core. Alternatively, the HEXPEDITE results show reasonable agreement with the majority of the CRP-5 calculations. Only the Japanese results with the DELIGHT-CITATION system agree well with the experimental data.

Table 20. Isothermal temperature coefficients of reactivity for HTTR.

Temp. [K]	Experiment	WIMS-D/4 JAR	DELIGHT CITATION	APOLLO2 CRONOS2	DRAGON HEXPEDITE PR-I	DRAGON HEXPEDITE PR-II
320	—	-2.33E-4	-1.19E-4*	-1.68E-4	-1.72E-04	-1.77E-04
345.55	-1.23E-4	—	—	—	—	—
360	—	-2.19E-4	-1.32E-4	-1.61E-4	-1.73E-04	-1.82E-04
400	—	-1.97E-4	-1.33E-4	-1.62E-4	-1.75E-04	-1.82E-04
406.65	-1.32E-4	—	—	—	—	—
440	—	-1.82E-4	-1.34E-4	-1.64E-4	-1.72E-04	-1.78E-04
470	—	-1.81E-4	-1.39E-4	-1.56E-4	-1.72E-04	-1.78E-04

* Interpolated value

8. ADVANCED CONCEPTS FOR CROSS-SECTION GENERATION

One of the main issues with the generation of cross-section in HTRs is the strong coupling between the blocks. This strong coupling invalidates the assumption made in the lattice physics calculation (identical neighbors in an infinite domain). In order to take the neighbor effects into account, a set of DRAGON 4 calculations was performed to determine the decoupling distance in HTTR. Figure 34 shows the variation in the neutron energy spectrum as the domain size increases. The four-ring model is equivalent to one single block. The 12-ring block is a two-block model, which with reflective boundary conditions constitutes an even larger domain.

The decoupled domain in HTTR is more than two rings of blocks beyond the domain of interest, i.e., cross-section generation domain. In some regions this extends beyond the permanent reflector. In an ideal situation one would attempt to generate the cross-sections from a 12th, 6th, or full-core calculation that would consider all neighbor effects. This is no easy task for the cross-section generator currently available. Alternatively, one could use an improved coarse energy structure and a much reduced calculation domain that allows capturing the majority of the spectral effects, which seem to occur in the first few blocks.

Therefore, in order to obtain better estimates of the energy flux, a supercell must include at least 19 blocks. This issue is specific to graphite moderated reactors, which contain fuel and reflector blocks with long migration areas. Table 21 shows the impact of the domain size on the one-group macroscopic cross-sections.
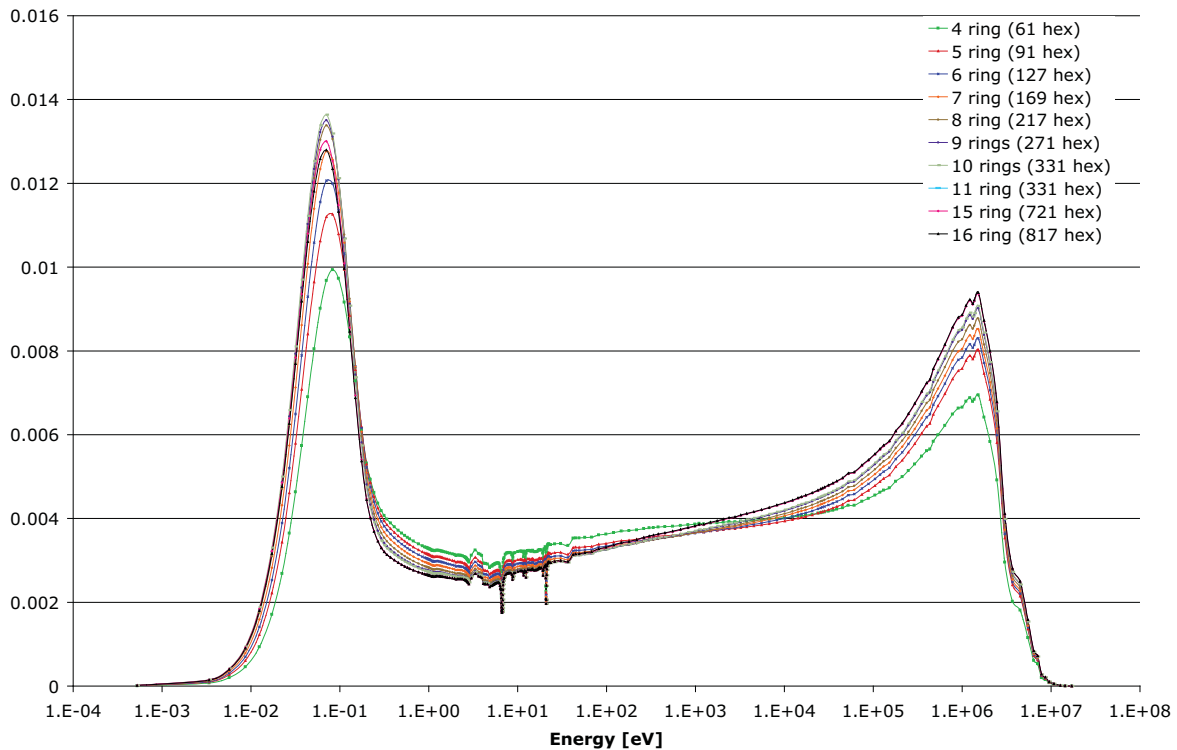

Figure 34. Change in the neutron spectrum as the domain size increases.

53

Table 21. One-group macroscopic cross-sections.

	Total	Absorption	NUSIGF	Scattering
Block	3.473E-01	2.697E-03	3.827E-03	3.446E-01
Decoupled	3.445E-01	3.123E-03	4.630E-03	3.414E-01
% Difference	−0.8%	13.6%	17.4%	−0.9%

9. CONCLUSIONS AND RECOMENDATIONS FOR FUTURE WORK

The analysis of the HTTR is a significant challenge for current deterministic methods since they were developed for the analysis of light water reactor (LWR) and fast reactor designs. HTR reactors exhibit neutron physics characteristics that lay between those of light water and fast reactors. In HTRs, especially in annular designs, neutrons travel significant distances. This creates a strong coupling between neighbors and, consequently, invalidates the assumptions made in traditional infinite lattice calculations during the generation of cross-sections. This "spectral interpenetration" can be approximated by using a finer group structure in the full-core calculation, as performed in this work, but the question of accuracy remains unresolved. A preliminary domain de-coupling study included in this work has shown that there can be significant errors if the neighbor effects are not considered in the cross-section generation step for a one group structure. These errors are somewhat alleviated by using the finer group structure, but a comprehensive study is needed to determine if combining a larger domain at the lattice level with a fine group structure in the condensation step can provide high fidelity cross-sections for the full core solver.

In addition to the complexities of HTR physics, the HTTR exhibits some special characteristics that further complicate the analysis of the reactor with deterministic methods. The major challenges are the presence of axial heterogeneities in the BP regions and the strong axial streaming in CR channels. There was no attempt in this study to directly address these effects, because they are not significant in the current NGNP design and there is uncertainty with regard to the fidelity of the data currently available from the HTTR experiment. Instead, a correction was applied to the final calculations. The use of these large corrections obscures the comparisons to other methods of analysis and the experimental data. If better HTTR data is available in the future to validate NGNP neutronic codes these two effects need to be addressed. To better model the axial heterogeneities in this reactor, two potential options are available: 1) decompose the block in axially homogeneous regions, or 2) perform a 3-D calculation for the BP region. The first option can be conducted with most cross-section generators available, but DRAGON 4 is the only lattice physics code known to the author that includes 3-D capability. Unfortunately, it is still experimental in nature and requires future development. Various lattice physics codes, including DRAGON 4, feature some capability to treat axial streaming effects via generation anisotropic diffusion coefficients. The method might need to be improved to accurately model the large diameter CR holes in the HTTR, since it was initially developed for smaller diameters holes.

This report shows that there are significant discrepancies between the MCNP5 and the DRAGON 4 results at the block level when the coated particles and BPs are modeled. These discrepancies can be resolved with comparisons to other cross-section generators. Nevertheless, the values of the multiplication factor obtained in this report show reasonable agreement with MCNP5 for the two critical configurations analyzed. Unfortunately, there seems to be a systematic bias of 2–3% common to all methods of solution, when compared to the experimental values, which is believed to stem from the cross-section data. Furthermore, the generation of cross-sections for the permanent reflector region of HTRs is an area that requires some investigation due to its significant impact of 0.5% Δk in HTTR.

These results from the deterministic codes can be further improved with more accurate modeling of the axial heterogeneity, axial streaming, radial positioning of the BP pins in the whole core model, and the use of more advanced cross-section generation techniques applicable to these reactors.

The cross-sections generated with SERPENT proved to be unreliable for this calculation. A thorough examination of this capability is recommended, since SERPENT is in an early state of development and shows great promise. Its applicability to HTR code benchmarking remains undetermined.

In summary, the recommendations arising from this work are as follows:

1) Determine the nature of the discrepancy between the MCNP5 and DRAGON 4 fuel block models by generating comparisons with other lattice codes, i.e. HELIOS, SCALE-6.

2) Setforth a significant effort in the study of cross-section generation techniques for prismatic HTRs with annular cores. This should include both fuel and non-multiplying regions. One option is extending the study included in section 8 by combining the larger domains at the lattice level with a fine group structure.

3) Research the generation of representative equivalence theory parameters for HTRs with annular cores. Include these equivalence theory parameters in the core solver in future studies to better represent the actual reaction rates.

4) Update the MCNP5 and SERPENT models with the latest as-built information to generate better comparisons to the experiment and the models developed in this work.

5) Include a representation of the axial streaming and axial heterogeneities in the whole core model.

6) Initiate comparisons of the flux and power shapes, both in code-to-code and experimental comparisons.

7) Further investigate the SERPENT cross-section generation capability for HTRs by comparison to other lattice codes, i.e. HELIOS, SCALE-6.

8) Investigate the accuracy of the current modeling method to describe the core boundary for the NGNP reactor. If necessary, modify current methods for the core solvers to better model or approximate the cylindrical boundary of the physical core.

10. REFERENCES

1. Oberkampf, W. L., 2009, "Perspectives on Verification, Validation, and Uncertainty Quantification," *SIAM Conference on Computational Science and Engineering, Miami, Florida, March 2–6, 2009*.

2. Terry, W.K., et. al., "Preliminary Assessment of Existing Experimental Data for Validation of Reactor Physics Codes and Data for NGNP Design and Analysis," ANL-05/05, September 2004.

3. IAEA, 2003, "Evaluation of High Temperature Gas Cooled Reactor Performance: Benchmark Analysis Related to Initial Testing of the HTTR and HTR-10," IAEA-TECDOC-1382.

4. Nojiri, N., et al., 1998, "Benchmark Problems' Data for the HTTR's Start-up Core Physics Experiments," JAERI memo 10-005, January 1998.

5. Bess, J. D., and N. Fujimoto, "Evaluation of the Start-Up Core Physics Tests at Japan's High Temperature Engineering Test Reactor (Fully Loaded Core)," HTTR-GCR-RESR-001, *International Handbook of Evaluated Reactor Physics Benchmark Experiments*, NEA/NSC/DOC(2006)1, OECD-NEA, March 2009.

6. Bess, J. D., and N. Fujimoto, "Evaluation of the Start-Up Core Physics Tests at Japan's High Temperature Engineering Test Reactor (Annular Core Loadings)," HTTR-GCR-RESR-002, *International Handbook of Evaluated Reactor Physics Benchmark Experiments*, NEA/NSC/DOC(2006)1, OECD- NEA, March 2009.

7. Kim, T.K., et al., "Whole-Core Depletion Studies in Support of Fuel Specification for the Next Generation Nuclear Plant (NGNP) Core," July 2004.

8. Lee, C.H., et al., "Status of Reactor Physics Activites on Cross Section Generation and Functionalization for the Prismatic Very High Temperature Reactor, and Development of Spatially-Heterogeneous Codes,"ANL-GenIV-075, August 2006.

9. Kim, K.S., et al., "Development of a physics analysis procedure for the prismatic very high temperature gas-cooled reactors," *Annals of Nuclear Energy*, Vol. 34, pp. 849, (2007).

10. Marleau, G., A. Hébert, and R. Roy, 2010, "A User Guide for Dragon Version4," Technical Report IGE–294, École Polytechnique de Montréal.

11. Fitzpatrick, W. E. and Ougouag, A. M., "HEXPEDITE: A Net Current Multigroup Nodal Diffusion Method for Hexagonal-z Geometry", *Trans. Am. Nucl. Soc.,* Vol. 66, 1992.

12. Ougouag, A. M. and Fitzpatrick, W. E., "An Inherently Parallel Multigroup Nodal Diffusion Method for Hexagonal-Z Geometry", *Fourth International Conference on Simulation Methods in Nuclear Engineering,* June 2-4, Montreal, Canada. (1993).

13. Fitzpatrick, W. E., "Developments in Nodal Reactor Analysis Tools for Hexagonal Geometry," Ph.D. Dissertation, University of Illinois at Urbana-Champaign. (1995)

14. Raepsaet, X., et al., "Analysis of the European Results on the HTTR's Core Physics Benchmarks," *Nucl. Eng. and Design*, Vol. 222, pp. 173–187 (2003).

15. Taiwo, T. A., and T. K. Kim, 2005, "Evaluation of the DRAGON code for VHTR Design and Analysis," ANL-GenIV-060, September 2005.

16. E. E. Lewis, C. B. Carrico, G. Palmiotti, "Variational Nodal Formulation for the Spherical Harmonic Equations," Nucl. Sci. Eng. 122, 194 (1996).

17. W. S. Yang, G. Palmiotti, and E.E. Lewis, "Numerical Optimization of Computing Algorithms of the Variational Nodal Method Based on Transformation of Variables" Nucl. Sci. and Eng. 139,174-185, (2001).

18. Brown, F. B., et al., 2002, "MCNP Version 5," LA-UR-02-3935, Los Alamos National Laboratory.

19. Leppänen, J., 2007, "Randomly Dispersed Particle Fuel Model in the PSG Monte Carlo Neutron Transport Code," In *Proc. M&C + SNA 2007, Monterey, California, April 15–19, 2007*.

20. Leppänen, J., 2007, "Development of a New Monte Carlo Reactor Physics Code," D.Sc. Thesis, Helsinki University of Technology, VTT Publications 640.

21. Goto, Minoru, et al., 2006, "Neutronics Calculations of HTTR with Several Nuclear Data Libraries," *J. Nuc. Scien. Tech.*, Vol. 43, N. 10, pp. 1237–1244.

22. Becker, et al., 2009, "Improvements of the Resonance Scattering Treatment in MCNP in View of HTR Calculations," *Ann. Nucl. Energy*, Vol. 36, pp. 281–285.

11. BIBLIOGRAPHY

Massimo, L., 1976, *Physics of High-Temperature Reactors*, New York: Pergamon Press.

Lee, C. H., et al., 2006, "Enhancement of REBUS-3/DIF3D for Whole-Core Neutronic Analysis of Prismatic Very High Temperature Reactor (VHTR)," ANL-GenIV-076, September 2006.

Appendix A

HTTR Annular Core Model

Appendix A

HTTR Annular Core Model

The annular core loading that was used in the HEXPEDITE model is listed in Table A-1 through Table A-9. These tables include:

- All positions in the hex-plane

- The type of block design assigned to that position based on the JAERI memo [4]

- Spectrum from the R-Z calculation used in the generation of cross-sections

- The HEXPEDITE material number assigned.

Table A-1. Annular core configuration in the first axial level.

Position	TYPE	S	material	Position	TYPE	S	material
1A01	CR A 1/2	1	1	1B01	RR A 1 1/3	4	42
1C01	CR A 1/2	8	9	1B02	RR A 1 1/3	4	42
1C03	CR A 1/2	8	9	1B03	RR A 1 1/3	4	42
1C05	CR A 1/2	8	9	1B04	RR A 1 1/3	4	42
1C07	CR A 1/2	8	9	1B05	RR A 1 1/3	4	42
1C09	CR A 1/2	8	9	1B06	RR A 1 1/3	4	42
1C11	CR A 1/2	8	9	1C02	RR A 1 1/3	8	43
1E01	CR A 1/2	15	6	1C04	RR A 1 1/3	8	43
1E02	RR D 1/4	15	56	1C06	RR A 1 1/3	8	43
1E03	CR A 1/2	15	2	1C08	RR A 1 1/3	8	43
1E04	RR D 1/4	15	56	1C10	RR A 1 1/3	8	43
1E05	RR D 2/4	15	59	1C12	RR A 1 1/3	8	43
1E06	RR D 1/4	15	56	1D01	RR A 2 1/3	8	48
1E07	CR A 1/2	15	2	1D02	RR A 2 1/3	8	48
1E08	RR D 1/4	15	56	1D03	RR A 2 1/3	8	48
1E09	CR A 1/2	15	6	1D04	RR A 2 1/3	8	48
1E10	RR D 1/4	15	56	1D05	RR A 2 1/3	8	48
1E11	CR A 1/2	15	2	1D06	RR A 2 1/3	8	48
1E12	RR D 1/4	15	56	1D07	RR A 2 1/3	8	48
1E13	RR D 2/4	15	59	1D08	RR A 2 1/3	8	48
1E14	RR D 1/4	15	56	1D09	RR A 2 1/3	8	48
1E15	CR A 1/2	15	2	1D10	RR A 2 1/3	8	48
1E16	RR D 1/4	15	56	1D11	RR A 2 1/3	8	48
1E17	CR A 1/2	15	6	1D12	RR A 2 1/3	8	48
1E18	RR D 1/4	15	56	1D13	RR A 2 1/3	8	48
1E19	CR A 1/2	15	2	1D14	RR A 2 1/3	8	48
1E20	RR D 1/4	15	56	1D15	RR A 2 1/3	8	48
1E21	RR D 2/4	15	59	1D16	RR A 2 1/3	8	48
1E22	RR D 1/4	15	56	1D17	RR A 2 1/3	8	48
1E23	CR A 1/2	15	2	1D18	RR A 2 1/3	8	48
1E24	RR D 1/4	15	56				

Table A-2. Annular core configuration in the second axial level.

Position	TYPE	S	material	Position	TYPE	S	material
2A01	CR A 1/2	1	1	2B01	RR A 1 2/3	4	44
2C01	CR A 1/2	8	9	2B02	RR A 1 2/3	4	44
2C03	CR A 1/2	8	9	2B03	RR A 1 2/3	4	44
2C05	CR A 1/2	8	9	2B04	RR A 1 2/3	4	44
2C07	CR A 1/2	8	9	2B05	RR A 1 2/3	4	44
2C09	CR A 1/2	8	9	2B06	RR A 1 2/3	4	44
2C11	CR A 1/2	8	9	2C02	RR A 1 2/3	8	45
2E01	CR A 1/2	15	6	2C04	RR A 1 2/3	8	45
2E02	RR D 1/4	15	56	2C06	RR A 1 2/3	8	45
2E03	CR A 1/2	15	2	2C08	RR A 1 2/3	8	45
2E04	RR D 1/4	15	56	2C10	RR A 1 2/3	8	45
2E05	RR D 2/4	15	59	2C12	RR A 1 2/3	8	45
2E06	RR D 1/4	15	56	2D01	RR A 2 2/3	8	49
2E07	CR A 1/2	15	2	2D02	RR A 2 2/3	8	49
2E08	RR D 1/4	15	56	2D03	RR A 2 2/3	8	49
2E09	CR A 1/2	15	6	2D04	RR A 2 2/3	8	49
2E10	RR D 1/4	15	56	2D05	RR A 2 2/3	8	49
2E11	CR A 1/2	15	2	2D06	RR A 2 2/3	8	49
2E12	RR D 1/4	15	56	2D07	RR A 2 2/3	8	49
2E13	RR D 2/4	15	59	2D08	RR A 2 2/3	8	49
2E14	RR D 1/4	15	56	2D09	RR A 2 2/3	8	49
2E15	CR A 1/2	15	2	2D10	RR A 2 2/3	8	49
2E16	RR D 1/4	15	56	2D11	RR A 2 2/3	8	49
2E17	CR A 1/2	15	6	2D12	RR A 2 2/3	8	49
2E18	RR D 1/4	15	56	2D13	RR A 2 2/3	8	49
2E19	CR A 1/2	15	2	2D14	RR A 2 2/3	8	49
2E20	RR D 1/4	15	56	2D15	RR A 2 2/3	8	49
2E21	RR D 2/4	15	59	2D16	RR A 2 2/3	8	49
2E22	RR D 1/4	15	56	2D17	RR A 2 2/3	8	49
2E23	CR A 1/2	15	2	2D18	RR A 2 2/3	8	49
2E24	RR D 1/4	15	56				

Table A-3. Annular core configuration in the third axial level.

Position	TYPE	S	material	Position	TYPE	S	material
3A01	CR A 1/2	1	1	3B01	DB A	4	27
3C01	CR A 2/2	9	11	3B02	Sim B	4	67
3C03	CR A 1/2	9	10	3B03	DB A	4	27
3C05	CR A 2/2	9	11	3B04	Sim B	4	67
3C07	CR A 1/2	9	10	3B05	DB A	4	27
3C09	CR A 2/2	9	11	3B06	Sim B	4	67
3C11	CR A 1/2	9	10	3C02	f793320		39
3E01	CR A 1/2	15	6	3C04	Sim B	9	69
3E02	RR D 1/4	15	56	3C06	Sim B	9	69
3E03	CR A 1/2	15	6	3C08	Sim B	9	69
3E04	RR D 1/4	15	56	3C10	Sim B	9	69
3E05	RR D 2/4	15	59	3C12	Sim B	9	69
3E06	RR D 1/4	15	56	3D01	f993120		41
3E07	CR A 1/2	15	6	3D02	f943120		40
3E08	RR D 1/4	15	56	3D03	f943120		40
3E09	CR A 1/2	15	6	3D04	f993120		41
3E10	RR D 1/4	15	56	3D05	f943120		40
3E11	CR A 1/2	15	6	3D06	f943120		40
3E12	RR D 1/4	15	56	3D07	f993120		41
3E13	RR D 2/4	15	59	3D08	f943120		40
3E14	RR D 1/4	15	56	3D09	f943120		40
3E15	CR A 1/2	15	6	3D10	f993120		41
3E16	RR D 1/4	15	56	3D11	f943120		40
3E17	CR A 1/2	15	6	3D12	f943120		40
3E18	RR D 1/4	15	56	3D13	f993120		41
3E19	CR A 1/2	15	6	3D14	f943120		40
3E20	RR D 1/4	15	56	3D15	f943120		40
3E21	RR D 2/4	15	59	3D16	f993120		41
3E22	RR D 1/4	15	56	3D17	f943120		40
3E23	CR A 1/2	15	6	3D18	f943120		40
3E24	RR D 1/4	15	56				

Table A-4. Annular core configuration in the fourth axial level.

Position	TYPE	S	Material	Position	TYPE	S	Material
4A01	CR A 1/2	2	3	4B01	DB B-2	5	29
4C01	CR A 1/2	10	4	4B02	Sim B	5	68
4C03	CR A 1/2	10	4	4B03	CR Block(1)	5	15
4C05	CR A 1/2	10	4	4B04	Sim B	5	68
4C07	CR A 1/2	10	4	4B05	CR Block(1)	5	15
4C09	CR A 1/2	10	4	4B06	Sim B	5	68
4C11	CR A 1/2	10	4	4C02	f633325		36
4E01	CR A 1/2	16	7	4C04	Sim B	10	63
4E02	RR D 1/4	16	57	4C06	Sim B	10	63
4E03	CR A 1/2	16	7	4C08	Sim B	10	63
4E04	RR D 1/4	16	57	4C10	Sim B	10	63
4E05	RR D 2/4	16	60	4C12	Sim B	10	63
4E06	RR D 1/4	16	57	4D01	f793125		38
4E07	CR A 1/2	16	7	4D02	f723125		37
4E08	RR D 1/4	16	57	4D03	f723125		37
4E09	CR A 1/2	16	7	4D04	f793125		38
4E10	RR D 1/4	16	57	4D05	f723125		37
4E11	CR A 1/2	16	7	4D06	f723125		37
4E12	RR D 4/4	16	62	4D07	f793125		38
4E13	RR D 2/4	16	60	4D08	f723125		37
4E14	RR D 1/4	16	57	4D09	f723125		37
4E15	CR A 1/2	16	7	4D10	f793125		38
4E16	RR D 1/4	16	57	4D11	f723125		37
4E17	CR A 1/2	16	7	4D12	f723125		37
4E18	RR D 4/4	16	62	4D13	f793125		38
4E19	CR A 1/2	16	7	4D14	f723125		37
4E20	RR D 1/4	16	57	4D15	f723125		37
4E21	RR D 2/4	16	60	4D16	f793125		38
4E22	RR D 1/4	16	57	4D17	f723125		37
4E23	CR A 1/2	16	7	4D18	f723125		37
4E24	RR D 4/4	16	62				

Table A-5. Annular core configuration in the fifth axial level.

Position	TYPE	S	material	Position	TYPE	S	material
5A01	CR A 1/2	2	8	5B01	CR Block(2)	5	16
5C01	CR A 1/2	11	5	5B02	Sim B	5	68
5C03	CR A 1/2	11	5	5B03	CR Block(1)	5	15
5C05	CR A 1/2	11	5	5B04	Sim B	5	68
5C07	CR A 1/2	11	5	5B05	CR Block(1)	5	15
5C09	CR A 1/2	11	5	5B06	Sim B	5	68
5C11	CR A 1/2	11	5	5C02	f523325		33
5E01	CR A 1/2	16	7	5C04	Sim B	11	64
5E02	RR D 1/4	16	57	5C06	Sim B	11	64
5E03	CR A 1/2	16	7	5C08	Sim B	11	64
5E04	RR D 1/4	16	57	5C10	Sim B	11	64
5E05	RR D 2/4	16	60	5C12	Sim B	11	64
5E06	RR D 1/4	16	57	5D01	f633125		35
5E07	CR A 1/2	16	7	5D02	f593125		34
5E08	RR D 1/4	16	57	5D03	f593125		34
5E09	CR A 1/2	16	7	5D04	f633125		35
5E10	RR D 1/4	16	57	5D05	f593125		34
5E11	CR A 1/2	16	7	5D06	f593125		34
5E12	RR D 1/4	16	57	5D07	f633125		35
5E13	RR D 2/4	16	60	5D08	f593125		34
5E14	RR D 1/4	16	57	5D09	f593125		34
5E15	CR A 1/2	16	7	5D10	f633125		35
5E16	RR D 1/4	16	57	5D11	f593125		34
5E17	CR A 1/2	16	7	5D12	f593125		34
5E18	RR D 1/4	16	57	5D13	f633125		35
5E19	CR A 1/2	16	7	5D14	f593125		34
5E20	RR D 1/4	16	57	5D15	f593125		34
5E21	RR D 2/4	16	60	5D16	f633125		35
5E22	RR D 1/4	16	57	5D17	f593125		34
5E23	CR A 1/2	16	7	5D18	f593125		34
5E24	RR D 1/4	16	57				

Table A-6. Annular core configuration in the sixth axial level.

Positison	TYPE	S	material	Position	TYPE	S	material
6A01	CR B	2	14	6B01	CR Block(3)	5	17
6C01	CR B	12	12	6B02	Sim B	5	68
6C03	CR B	12	12	6B03	CR Block(1)	5	15
6C05	CR B	12	12	6B04	Sim B	5	68
6C07	CR B	12	12	6B05	CR Block(1)	5	15
6C09	CR B	12	12	6B06	Sim B	5	68
6C11	CR B	12	12	6C02	f393320		30
6E01	CR B	16	13	6C04	Sim B	12	65
6E02	RR D 1/4	16	57	6C06	Sim B	12	65
6E03	CR B	16	13	6C08	Sim B	12	65
6E04	RR D 1/4	16	57	6C10	Sim B	12	65
6E05	RR D 2/4	16	60	6C12	Sim B	12	65
6E06	RR D 1/4	16	57	6D01	f483120		32
6E07	CR B	16	13	6D02	f433120		31
6E08	RR D 1/4	16	57	6D03	f433120		31
6E09	CR B	16	13	6D04	f483120		32
6E10	RR D 1/4	16	57	6D05	f433120		31
6E11	CR B	16	13	6D06	f433120		31
6E12	RR D 1/4	16	57	6D07	f483120		32
6E13	RR D 2/4	16	60	6D08	f433120		31
6E14	RR D 1/4	16	57	6D09	f433120		31
6E15	CR B	16	13	6D10	f483120		32
6E16	RR D 1/4	16	57	6D11	f433120		31
6E17	CR B	16	13	6D12	f433120		31
6E18	RR D 1/4	16	57	6D13	f483120		32
6E19	CR B	16	13	6D14	f433120		31
6E20	RR D 1/4	16	57	6D15	f433120		31
6E21	RR D 2/4	16	60	6D16	f483120		32
6E22	RR D 1/4	16	57	6D17	f433120		31
6E23	CR B	16	13	6D18	f433120		31
6E24	RR D 1/4	16	57				

Table A-7. Annular core configuration in the seventh axial level.

Position	TYPE	S	material	Position	TYPE	S	material
7A01	CR C	3	20	7B01	DB B-1	5	28
7C01	CR C	13	18	7B02	Sim B	5	68
7C03	CR C	13	18	7B03	DB B-1	5	28
7C05	CR C	13	18	7B04	Sim B	5	68
7C07	CR C	13	18	7B05	DB B-1	5	28
7C09	CR C	13	18	7B06	Sim B	5	68
7C11	CR C	13	18	7C02	f393320		30
7E01	CR C	16	19	7C04	Sim B	13	66
7E02	RR D 1/4	16	57	7C06	Sim B	13	66
7E03	CR C	16	19	7C08	Sim B	13	66
7E04	RR D 1/4	16	57	7C10	Sim B	13	66
7E05	RR D 3/4	16	61	7C12	Sim B	13	66
7E06	RR D 1/4	16	57	7D01	f483120		32
7E07	CR C	16	19	7D02	f433120		31
7E08	RR D 1/4	16	57	7D03	f433120		31
7E09	CR C	16	19	7D04	f483120		32
7E10	RR D 1/4	16	57	7D05	f433120		31
7E11	CR C	16	19	7D06	f433120		31
7E12	RR D 1/4	16	57	7D07	f483120		32
7E13	RR D 3/4	16	61	7D08	f433120		31
7E14	RR D 1/4	16	57	7D09	f433120		31
7E15	CR C	16	19	7D10	f483120		32
7E16	RR D 1/4	16	57	7D11	f433120		31
7E17	CR C	16	19	7D12	f433120		31
7E18	RR D 1/4	16	57	7D13	f483120		32
7E19	CR C	16	19	7D14	f433120		31
7E20	RR D 1/4	16	57	7D15	f433120		31
7E21	RR D 3/4	16	61	7D16	f483120		32
7E22	RR D 1/4	16	57	7D17	f433120		31
7E23	CR C	16	19	7D18	f433120		31
7E24	RR D 1/4	16	57				

Table A-8. Annular core configuration in the eighth axial level.

Position	TYPE	S	material	Position	TYPE	S	material
8A01	CR D	3	23	8B01	RR A 1 3/3	6	47
8C01	CR D	14	21	8B02	RR A 1 3/3	6	47
8C03	CR D	14	21	8B03	RR A 1 3/3	6	47
8C05	CR D	14	21	8B04	RR A 1 3/3	6	47
8C07	CR D	14	21	8B05	RR A 1 3/3	6	47
8C09	CR D	14	21	8B06	RR A 1 3/3	6	47
8C11	CR D	14	21	8C02	RR A 1 3/3	14	46
8E01	CR D	17	22	8C04	RR A 1 3/3	14	46
8E02	RR D 1/4	17	58	8C06	RR A 1 3/3	14	46
8E03	CR D	17	22	8C08	RR A 1 3/3	14	46
8E04	RR D 1/4	17	58	8C10	RR A 1 3/3	14	46
8E05	RR D 1/4	17	58	8C12	RR A 1 3/3	14	46
8E06	RR D 1/4	17	58	8D01	RR A 2 3/3	14	50
8E07	CR D	17	22	8D02	RR A 2 3/3	14	50
8E08	RR D 1/4	17	58	8D03	RR A 2 3/3	14	50
8E09	CR D	17	22	8D04	RR A 2 3/3	14	50
8E10	RR D 1/4	17	58	8D05	RR A 2 3/3	14	50
8E11	CR D	17	22	8D06	RR A 2 3/3	14	50
8E12	RR D 1/4	17	58	8D07	RR A 2 3/3	14	50
8E13	RR D 1/4	17	58	8D08	RR A 2 3/3	14	50
8E14	RR D 1/4	17	58	8D09	RR A 2 3/3	14	50
8E15	CR D	17	22	8D10	RR A 2 3/3	14	50
8E16	RR D 1/4	17	58	8D11	RR A 2 3/3	14	50
8E17	CR D	17	22	8D12	RR A 2 3/3	14	50
8E18	RR D 1/4	17	58	8D13	RR A 2 3/3	14	50
8E19	CR D	17	22	8D14	RR A 2 3/3	14	50
8E20	RR D 1/4	17	58	8D15	RR A 2 3/3	14	50
8E21	RR D 1/4	17	58	8D16	RR A 2 3/3	14	50
8E22	RR D 1/4	17	58	8D17	RR A 2 3/3	14	50
8E23	CR D	17	22	8D18	RR A 2 3/3	14	50
8E24	RR D 1/4	17	58				

Table A-9. Annular core configuration in the ninth axial level.

Position	TYPE	S	material	Position	TYPE	S	material
9A01	CR E 1/2	3	24	9B01	RR B 2/2	7	53
9C01	CR E 2/2	14	25	9B02	RR B 2/2	7	53
9C03	CR E 2/2	14	25	9B03	RR B 2/2	7	53
9C05	CR E 2/2	14	25	9B04	RR B 2/2	7	53
9C07	CR E 2/2	14	25	9B05	RR B 2/2	7	53
9C09	CR E 2/2	14	25	9B06	RR B 2/2	7	53
9C11	CR E 2/2	14	25	9C02	RR B 2/2	14	52
9E01	CR E 2/2	18	26	9C04	RR B 2/2	14	52
9E02	RR C 1/2	18	54	9C06	RR B 2/2	14	52
9E03	CR E 2/2	18	26	9C08	RR B 2/2	14	52
9E04	RR C 1/2	18	54	9C10	RR B 2/2	14	52
9E05	RR C 2/2	18	55	9C12	RR B 2/2	14	52
9E06	RR C 1/2	18	54	9D01	RR B 2/2	14	52
9E07	CR E 2/2	18	26	9D02	RR B 1/2	14	51
9E08	RR C 1/2	18	54	9D03	RR B 1/2	14	51
9E09	CR E 2/2	18	26	9D04	RR B 2/2	14	52
9E10	RR C 1/2	18	54	9D05	RR B 1/2	14	51
9E11	CR E 2/2	18	26	9D06	RR B 1/2	14	51
9E12	RR C 1/2	18	54	9D07	RR B 2/2	14	52
9E13	RR C 2/2	18	55	9D08	RR B 1/2	14	51
9E14	RR C 1/2	18	54	9D09	RR B 1/2	14	51
9E15	CR E 2/2	18	26	9D10	RR B 2/2	14	52
9E16	RR C 1/2	18	54	9D11	RR B 1/2	14	51
9E17	CR E 2/2	18	26	9D12	RR B 1/2	14	51
9E18	RR C 1/2	18	54	9D13	RR B 2/2	14	52
9E19	CR E 2/2	18	26	9D14	RR B 1/2	14	51
9E20	RR C 1/2	18	54	9D15	RR B 1/2	14	51
9E21	RR C 2/2	18	55	9D16	RR B 2/2	14	52
9E22	RR C 1/2	18	54	9D17	RR B 1/2	14	51
9E23	CR E 2/2	18	26	9D18	RR B 1/2	14	51
9E24	RR C 1/2	18	54				

Appendix B

HTTR Fully Loaded Core Model

Appendix B

HTTR Fully Loaded Core Model

The fully loaded core loading that was used in the HEXPEDITE model is listed in Table B-1 through Table B-9Table . These tables include:

- All positions in the hex-plane
- The type of block design assigned to that position based on the JAERI memo [4]
- The HEXPEDITE material number assigned.

Table B-1. Fully loaded core configuration in the first axial level.

Position	TYPE	mat #	Position	TYPE	mat #
1A01	CR A 1/2 C	3	1B01	RR A 1 1/3	25
1C01	CR A 1/2 C	3	1B02	RR A 1 1/3	25
1C03	CR A 1/2 C	3	1B03	RR A 1 1/3	25
1C05	CR A 1/2 C	3	1B04	RR A 1 1/3	25
1C07	CR A 1/2 C	3	1B05	RR A 1 1/3	25
1C09	CR A 1/2 C	3	1B06	RR A 1 1/3	25
1C11	CR A 1/2 C	3	1C02	RR A 1 1/3	25
1E01	CR A 1/2	1	1C04	RR A 1 1/3	25
1E02	RR D 1/4	35	1C06	RR A 1 1/3	25
1E03	CR A 1/2 C	3	1C08	RR A 1 1/3	25
1E04	RR D 1/4	35	1C10	RR A 1 1/3	25
1E05	RR D 2/4	36	1C12	RR A 1 1/3	25
1E06	RR D 1/4	35	1D01	RR A 2 1/3	28
1E07	CR A 1/2 C	3	1D02	RR A 2 1/3	28
1E08	RR D 1/4	35	1D03	RR A 2 1/3	28
1E09	CR A 1/2	1	1D04	RR A 2 1/3	28
1E10	RR D 1/4	35	1D05	RR A 2 1/3	28
1E11	CR A 1/2 C	3	1D06	RR A 2 1/3	28
1E12	RR D 1/4	35	1D07	RR A 2 1/3	28
1E13	RR D 2/4	36	1D08	RR A 2 1/3	28
1E14	RR D 1/4	35	1D09	RR A 2 1/3	28
1E15	CR A 1/2 C	3	1D10	RR A 2 1/3	28
1E16	RR D 1/4	35	1D11	RR A 2 1/3	28
1E17	CR A 1/2	1	1D12	RR A 2 1/3	28
1E18	RR D 1/4	35	1D13	RR A 2 1/3	28
1E19	CR A 1/2 C	3	1D14	RR A 2 1/3	28
1E20	RR D 1/4	35	1D15	RR A 2 1/3	28
1E21	RR D 2/4	36	1D16	RR A 2 1/3	28
1E22	RR D 1/4	35	1D17	RR A 2 1/3	28
1E23	CR A 1/2 C	3	1D18	RR A 2 1/3	28
1E24	RR D 1/4	35			

Table B-2. Fully loaded core configuration in the second axial level.

Position	TYPE	mat #		TYPE	mat #
2A01	CR A 1/2 C	3	2B01	RR A 1 2/3	26
2C01	CR A 1/2 C	3	2B02	RR A 1 2/3	26
2C03	CR A 1/2 C	3	2B03	RR A 1 2/3	26
2C05	CR A 1/2 C	3	2B04	RR A 1 2/3	26
2C07	CR A 1/2 C	3	2B05	RR A 1 2/3	26
2C09	CR A 1/2 C	3	2B06	RR A 1 2/3	26
2C11	CR A 1/2 C	3	2C02	RR A 1 2/3	26
2E01	CR A 1/2	1	2C04	RR A 1 2/3	26
2E02	RR D 1/4	35	2C06	RR A 1 2/3	26
2E03	CR A 1/2 C	3	2C08	RR A 1 2/3	26
2E04	RR D 1/4	35	2C10	RR A 1 2/3	26
2E05	RR D 2/4	36	2C12	RR A 1 2/3	26
2E06	RR D 1/4	35	2D01	RR A 2 2/3	29
2E07	CR A 1/2 C	3	2D02	RR A 2 2/3	29
2E08	RR D 1/4	35	2D03	RR A 2 2/3	29
2E09	CR A 1/2	1	2D04	RR A 2 2/3	29
2E10	RR D 1/4	35	2D05	RR A 2 2/3	29
2E11	CR A 1/2 C	3	2D06	RR A 2 2/3	29
2E12	RR D 1/4	35	2D07	RR A 2 2/3	29
2E13	RR D 2/4	36	2D08	RR A 2 2/3	29
2E14	RR D 1/4	35	2D09	RR A 2 2/3	29
2E15	CR A 1/2 C	3	2D10	RR A 2 2/3	29
2E16	RR D 1/4	35	2D11	RR A 2 2/3	29
2E17	CR A 1/2	1	2D12	RR A 2 2/3	29
2E18	RR D 1/4	35	2D13	RR A 2 2/3	29
2E19	CR A 1/2 C	3	2D14	RR A 2 2/3	29
2E20	RR D 1/4	35	2D15	RR A 2 2/3	29
2E21	RR D 2/4	36	2D16	RR A 2 2/3	29
2E22	RR D 1/4	35	2D17	RR A 2 2/3	29
2E23	CR A 1/2 C	3	2D18	RR A 2 2/3	29
2E24	RR D 1/4	35			

Table B-3. Fully loaded core configuration in the third axial level.

Position	TYPE	mat #	Position	TYPE	mat #
3A01	CR A 1/2 C	3	3B01	f673320	19
3C01	CR A 2/2 C	4	3B02	f673320	19
3C03	CR A 1/2 C	3	3B03	f673320	19
3C05	CR A 2/2 C	4	3B04	f673320	19
3C07	CR A 1/2 C	3	3B05	f673320	19
3C09	CR A 2/2 C	4	3B06	f673320	19
3C11	CR A 1/2 C	3	3C02	f793320	22
3E01	CR A 1/2	1	3C04	f793320	22
3E02	RR D 1/4	35	3C06	f793320	22
3E03	CR A 1/2 C	3	3C08	f793320	22
3E04	RR D 1/4	35	3C10	f793320	22
3E05	RR D 2/4	36	3C12	f793320	22
3E06	RR D 1/4	35	3D01	f993120	24
3E07	CR A 1/2 C	3	3D02	f943120	23
3E08	RR D 1/4	35	3D03	f943120	23
3E09	CR A 1/2	1	3D04	f993120	24
3E10	RR D 1/4	35	3D05	f943120	23
3E11	CR A 1/2 C	3	3D06	f943120	23
3E12	RR D 1/4	35	3D07	f993120	24
3E13	RR D 2/4	36	3D08	f943120	23
3E14	RR D 1/4	35	3D09	f943120	23
3E15	CR A 1/2 C	3	3D10	f993120	24
3E16	RR D 1/4	35	3D11	f943120	23
3E17	CR A 1/2	1	3D12	f943120	23
3E18	RR D 1/4	35	3D13	f993120	24
3E19	CR A 1/2 C	3	3D14	f943120	23
3E20	RR D 1/4	35	3D15	f943120	23
3E21	RR D 2/4	36	3D16	f993120	24
3E22	RR D 1/4	35	3D17	f943120	23
3E23	CR A 1/2 C	3	3D18	f943120	23
3E24	RR D 1/4	35			

Table B-4. Fully loaded core configuration in the fourth axial level.

Position	TYPE	mat #	Position	TYPE	mat #
4A01	CR A 1/2 C	3	4B01	f523325	15
4C01	CR A 1/2 C	3	4B02	f523325	15
4C03	CR A 1/2 C	3	4B03	f523325	15
4C05	CR A 1/2 C	3	4B04	f523325	15
4C07	CR A 1/2 C	3	4B05	f523325	15
4C09	CR A 1/2 C	3	4B06	f523325	15
4C11	CR A 1/2 C	3	4C02	f633325	18
4E01	CR A 1/2	1	4C04	f633325	18
4E02	RR D 1/4	35	4C06	f633325	18
4E03	CR A 1/2 C	3	4C08	f633325	18
4E04	RR D 1/4	35	4C10	f633325	18
4E05	RR D 2/4	36	4C12	f633325	18
4E06	RR D 1/4	35	4D01	f793125	21
4E07	CR A 1/2 C	3	4D02	f723125	20
4E08	RR D 1/4	35	4D03	f723125	20
4E09	CR A 1/2	1	4D04	f793125	21
4E10	RR D 1/4	35	4D05	f723125	20
4E11	CR A 1/2 C	3	4D06	f723125	20
4E12	RR D 4/4	38	4D07	f793125	21
4E13	RR D 2/4	36	4D08	f723125	20
4E14	RR D 1/4	35	4D09	f723125	20
4E15	CR A 1/2 C	3	4D10	f793125	21
4E16	RR D 1/4	35	4D11	f723125	20
4E17	CR A 1/2	1	4D12	f723125	20
4E18	RR D 4/4	38	4D13	f793125	21
4E19	CR A 1/2 C	3	4D14	f723125	20
4E20	RR D 1/4	35	4D15	f723125	20
4E21	RR D 2/4	36	4D16	f793125	21
4E22	RR D 1/4	35	4D17	f723125	20
4E23	CR A 1/2 C	3	4D18	f723125	20
4E24	RR D 4/4	38			

Table B-5. Fully loaded core configuration in the fifth axial level.

Position	TYPE	mat #	Position	TYPE	mat #
5A01	CR A 1/2	1	5B01	f433325	13
5C01	CR A 1/2	1	5B02	f433325	13
5C03	CR A 1/2	1	5B03	f433325	13
5C05	CR A 1/2	1	5B04	f433325	13
5C07	CR A 1/2	1	5B05	f433325	13
5C09	CR A 1/2	1	5B06	f433325	13
5C11	CR A 1/2	1	5C02	f523325	15
5E01	CR A 1/2	1	5C04	f523325	15
5E02	RR D 1/4	35	5C06	f523325	15
5E03	CR A 1/2	1	5C08	f523325	15
5E04	RR D 1/4	35	5C10	f523325	15
5E05	RR D 2/4	36	5C12	f523325	15
5E06	RR D 1/4	35	5D01	f633125	17
5E07	CR A 1/2	1	5D02	f593125	16
5E08	RR D 1/4	35	5D03	f593125	16
5E09	CR A 1/2	1	5D04	f633125	17
5E10	RR D 1/4	35	5D05	f593125	16
5E11	CR A 1/2	1	5D06	f593125	16
5E12	RR D 1/4	35	5D07	f633125	17
5E13	RR D 2/4	36	5D08	f593125	16
5E14	RR D 1/4	35	5D09	f593125	16
5E15	CR A 1/2	1	5D10	f633125	17
5E16	RR D 1/4	35	5D11	f593125	16
5E17	CR A 1/2	1	5D12	f593125	16
5E18	RR D 1/4	35	5D13	f633125	17
5E19	CR A 1/2	1	5D14	f593125	16
5E20	RR D 1/4	35	5D15	f593125	16
5E21	RR D 2/4	36	5D16	f633125	17
5E22	RR D 1/4	35	5D17	f593125	16
5E23	CR A 1/2	1	5D18	f593125	16
5E24	RR D 1/4	35			

Table B-6. Fully loaded core configuration in the sixth axial level.

Position	TYPE	mat #	Position	TYPE	mat #
6A01	CR B	5	6B01	f343320	10
6C01	CR B	5	6B02	f343320	10
6C03	CR B	5	6B03	f343320	10
6C05	CR B	5	6B04	f343320	10
6C07	CR B	5	6B05	f343320	10
6C09	CR B	5	6B06	f343320	10
6C11	CR B	5	6C02	f393320	11
6E01	CR B	5	6C04	f393320	11
6E02	RR D 1/4	35	6C06	f393320	11
6E03	CR B	5	6C08	f393320	11
6E04	RR D 1/4	35	6C10	f393320	11
6E05	RR D 2/4	36	6C12	f393320	11
6E06	RR D 1/4	35	6D01	f483120	14
6E07	CR B	5	6D02	f433120	12
6E08	RR D 1/4	35	6D03	f433120	12
6E09	CR B	5	6D04	f483120	14
6E10	RR D 1/4	35	6D05	f433120	12
6E11	CR B	5	6D06	f433120	12
6E12	RR D 1/4	35	6D07	f483120	14
6E13	RR D 2/4	36	6D08	f433120	12
6E14	RR D 1/4	35	6D09	f433120	12
6E15	CR B	5	6D10	f483120	14
6E16	RR D 1/4	35	6D11	f433120	12
6E17	CR B	5	6D12	f433120	12
6E18	RR D 1/4	35	6D13	f483120	14
6E19	CR B	5	6D14	f433120	12
6E20	RR D 1/4	35	6D15	f433120	12
6E21	RR D 2/4	36	6D16	f483120	14
6E22	RR D 1/4	35	6D17	f433120	12
6E23	CR B	5	6D18	f433120	12
6E24	RR D 1/4	35			

Table B-7. Fully loaded core configuration in the seventh axial level.

Position	TYPE	mat #	Position	TYPE	mat #
7A01	CR C	6	7B01	f343320	10
7C01	CR C	6	7B02	f343320	10
7C03	CR C	6	7B03	f343320	10
7C05	CR C	6	7B04	f343320	10
7C07	CR C	6	7B05	f343320	10
7C09	CR C	6	7B06	f343320	10
7C11	CR C	6	7C02	f393320	11
7E01	CR C	6	7C04	f393320	11
7E02	RR D 1/4	35	7C06	f393320	11
7E03	CR C	6	7C08	f393320	11
7E04	RR D 1/4	35	7C10	f393320	11
7E05	RR D 3/4	37	7C12	f393320	11
7E06	RR D 1/4	35	7D01	f483120	14
7E07	CR C	6	7D02	f433120	12
7E08	RR D 1/4	35	7D03	f433120	12
7E09	CR C	6	7D04	f483120	14
7E10	RR D 1/4	35	7D05	f433120	12
7E11	CR C	6	7D06	f433120	12
7E12	RR D 1/4	35	7D07	f483120	14
7E13	RR D 3/4	37	7D08	f433120	12
7E14	RR D 1/4	35	7D09	f433120	12
7E15	CR C	6	7D10	f483120	14
7E16	RR D 1/4	35	7D11	f433120	12
7E17	CR C	6	7D12	f433120	12
7E18	RR D 1/4	35	7D13	f483120	14
7E19	CR C	6	7D14	f433120	12
7E20	RR D 1/4	35	7D15	f433120	12
7E21	RR D 3/4	37	7D16	f483120	14
7E22	RR D 1/4	35	7D17	f433120	12
7E23	CR C	6	7D18	f433120	12
7E24	RR D 1/4	35			

Table B-8. Fully loaded core configuration in the eight axial level.

Position	TYPE	mat #	Position	TYPE	mat #
8A01	CR D	7	8B01	RR A 1 3/3	27
8C01	CR D	7	8B02	RR A 1 3/3	27
8C03	CR D	7	8B03	RR A 1 3/3	27
8C05	CR D	7	8B04	RR A 1 3/3	27
8C07	CR D	7	8B05	RR A 1 3/3	27
8C09	CR D	7	8B06	RR A 1 3/3	27
8C11	CR D	7	8C02	RR A 1 3/3	27
8E01	CR D	7	8C04	RR A 1 3/3	27
8E02	RR D 1/4	35	8C06	RR A 1 3/3	27
8E03	CR D	7	8C08	RR A 1 3/3	27
8E04	RR D 1/4	35	8C10	RR A 1 3/3	27
8E05	RR D 1/4	35	8C12	RR A 1 3/3	27
8E06	RR D 1/4	35	8D01	RR A 2 3/3	30
8E07	CR D	7	8D02	RR A 2 3/3	30
8E08	RR D 1/4	35	8D03	RR A 2 3/3	30
8E09	CR D	7	8D04	RR A 2 3/3	30
8E10	RR D 1/4	35	8D05	RR A 2 3/3	30
8E11	CR D	7	8D06	RR A 2 3/3	30
8E12	RR D 1/4	35	8D07	RR A 2 3/3	30
8E13	RR D 1/4	35	8D08	RR A 2 3/3	30
8E14	RR D 1/4	35	8D09	RR A 2 3/3	30
8E15	CR D	7	8D10	RR A 2 3/3	30
8E16	RR D 1/4	35	8D11	RR A 2 3/3	30
8E17	CR D	7	8D12	RR A 2 3/3	30
8E18	RR D 1/4	35	8D13	RR A 2 3/3	30
8E19	CR D	7	8D14	RR A 2 3/3	30
8E20	RR D 1/4	35	8D15	RR A 2 3/3	30
8E21	RR D 1/4	35	8D16	RR A 2 3/3	30
8E22	RR D 1/4	35	8D17	RR A 2 3/3	30
8E23	CR D	7	8D18	RR A 2 3/3	30
8E24	RR D 1/4	35			

Table B-9. Fully loaded core configuration in the ninth axial level.

Position	TYPE	mat #	Position	TYPE	mat #
9A01	CR E 1/2	8	9B01	RR B 2/2	32
9C01	CR E 2/2	9	9B02	RR B 2/2	32
9C03	CR E 2/2	9	9B03	RR B 2/2	32
9C05	CR E 2/2	9	9B04	RR B 2/2	32
9C07	CR E 2/2	9	9B05	RR B 2/2	32
9C09	CR E 2/2	9	9B06	RR B 2/2	32
9C11	CR E 2/2	9	9C02	RR B 2/2	32
9E01	CR E 2/2	9	9C04	RR B 2/2	32
9E02	RR C 1/2	33	9C06	RR B 2/2	32
9E03	CR E 2/2	9	9C08	RR B 2/2	32
9E04	RR C 1/2	33	9C10	RR B 2/2	32
9E05	RR C 2/2	34	9C12	RR B 2/2	32
9E06	RR C 1/2	33	9D01	RR B 2/2	32
9E07	CR E 2/2	9	9D02	RR B 1/2	31
9E08	RR C 1/2	33	9D03	RR B 1/2	31
9E09	CR E 2/2	9	9D04	RR B 2/2	32
9E10	RR C 1/2	33	9D05	RR B 1/2	31
9E11	CR E 2/2	9	9D06	RR B 1/2	31
9E12	RR C 1/2	33	9D07	RR B 2/2	32
9E13	RR C 2/2	34	9D08	RR B 1/2	31
9E14	RR C 1/2	33	9D09	RR B 1/2	31
9E15	CR E 2/2	9	9D10	RR B 2/2	32
9E16	RR C 1/2	33	9D11	RR B 1/2	31
9E17	CR E 2/2	9	9D12	RR B 1/2	31
9E18	RR C 1/2	33	9D13	RR B 2/2	32
9E19	CR E 2/2	9	9D14	RR B 1/2	31
9E20	RR C 1/2	33	9D15	RR B 1/2	31
9E21	RR C 2/2	34	9D16	RR B 2/2	32
9E22	RR C 1/2	33	9D17	RR B 1/2	31
9E23	CR E 2/2	9	9D18	RR B 1/2	31
9E24	RR C 1/2	33			